J. Fluid Mech. (2025), *vol.* 1015, A51, doi:10.1017/jfm.2025.10213

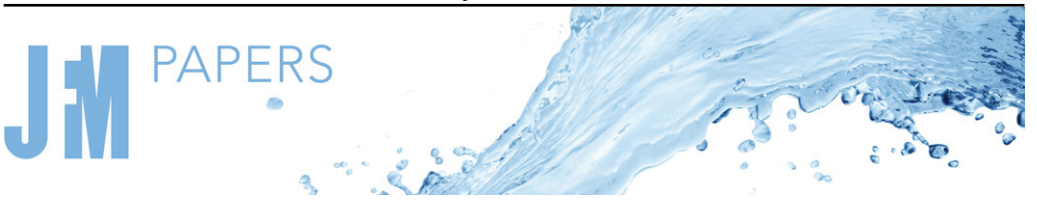

Characterisation of sea ice kinematics over oceanic eddies

Minki Kim[1], **Georgy E. Manucharyan**[2] **and Monica M. Wilhelmus**[1]

[1]Center for Fluid Mechanics, School of Engineering, Brown University, Providence, RI 02912, USA

[2]School of Oceanography, University of Washington, Seattle, WA, USA

Corresponding author: Monica M. Wilhelmus, mmwilhelmus@brown.edu

(Received 19 November 2024; revised 18 March 2025; accepted 28 April 2025)

Eddies within the meso/submeso-scale range are prevalent throughout the Arctic Ocean, playing a pivotal role in regulating the freshwater budget, heat transfer and sea ice transport. While observations have suggested a strong connection between the dynamics of sea ice and the underlying turbulent flows, quantifying this relationship remains an ambitious task due to the challenges of acquiring concurrent sea ice and ocean measurements. Recently, an innovative study using a unique algorithm to track sea ice floes showed that ice floes can be used as vorticity-meters of the ocean. Here, we present a numerical and analytical evaluation of this result by estimating the kinematic link between free-drifting ice floes and underlying ocean eddies using idealised vortex models. These analyses are expanded to explore local eddies in quasi-geostrophic turbulence, providing a more realistic representation of eddies in the Arctic Ocean. We find that in both flow fields, the relationship between floe rotation rates and ocean vorticity depends on the relative size of the ice floe to the eddy. As the floe size approaches and exceeds the eddy size, the floe rotation rates depart from half of the ocean vorticity. Finally, the effects of ice floe thickness, atmospheric winds and floe collisions on floe rotations are investigated. The derived relations and floe statistics set the foundation for leveraging remote sensing observations of floe motions to characterise eddy vorticity at small to moderate scales. This innovative approach opens new possibilities for quantifying Arctic Ocean eddy characteristics, providing valuable inputs for more accurate climate projections.

Key words: sea ice, quasi-geostrophic flows

1. Introduction

Mesoscale and submesoscale oceanic eddies, ranging from 10 to 300 km and 0.2 to 20 km, respectively, are widespread throughout the global ocean. These coherent structures are known to contain approximately 80 % of the ocean kinetic energy (Ferrari & Wunsch 2009; Klein *et al.* 2019), influencing global ocean circulation, biogeochemical tracer transport and energy transfer across various length scales. Ocean variability at mesoscales typically follows the principles of geostrophic turbulence, characterised by an inverse energy cascade that strengthens larger eddies and redistributes kinetic energy and by a forward-enstrophy cascade that creates finer filament features in the flow (Boffetta & Ecke 2012; Callies & Ferrari 2013; Klein *et al.* 2019). In ice-covered regions, such as the Arctic Ocean, the characteristics of ocean turbulence are strongly affected by ice-ocean interactions; oceanic eddies contribute to sea ice melting by enhancing vertical mixing and transporting heat from deeper ocean layers to the surface (Horvat, Tziperman & Campin 2016; Gupta & Thompson 2022; Manucharyan & Thompson 2022). In addition, atmosphere–sea ice–ocean interactions lead to momentum and heat exchanges, resulting in increased dissipation of eddy kinetic energy due to sea ice–ocean drag (Liu *et al.* 2024; Müller *et al.* 2024).

With the continued global warming trend, the Arctic sea ice cover has experienced changes in its characteristics and a rapid decline in its extent (Kwok & Rothrock 2009; Rampal, Weiss & Marsan 2009; Comiso 2012). As a result, Arctic marginal ice zones (MIZ) – the transitional regions between dense pack ice and open ocean – have become more prominent (Strong & Rigor 2013; Rolph, Feltham & Schröder 2020), fostering more energetic mesoscale variability in the ocean (Armitage *et al.* 2020; von Appen *et al.* 2022), and intensifying eddy fields (Manucharyan, Lopez-Acosta & Wilhelmus 2022). However, the variability of MIZ eddies and their relation to sea ice are yet to be fully characterised, partly due to the challenges of acquiring observations in ice-covered regions. On the one hand, while *in situ* eddy observations, such as those acquired via ice-tethered profilers (Timmermans *et al.* 2008; Zhao *et al.* 2016) and moorings (Zhao *et al.* 2016; Pnyushkov *et al.* 2018; Cassianides, Lique & Korosov 2021), provide accurate, temporally resolved data, measurements remain sparse and mostly out of MIZ. On the other hand, remote sensing techniques, including satellite altimetry, offer broader spatial coverage and allow for a more comprehensive characterisation of the eddy field (Kozlov *et al.* 2019; Kozlov, Plotnikov & Manucharyan 2020; Kubryakov, Kozlov & Manucharyan 2021). But, processing data in ice-covered areas remains challenging, limiting analyses to seasonally ice-free regions. In addition, satellite altimeters acquire measurements infrequently and with limited spatial coverage at high latitudes, where the Rossby deformation radius is smaller compared with lower latitudes. Notably, the recent launch of the Surface Water and Ocean Topography (SWOT) satellite, with $O(1$ km) spatial resolution, promises more detailed surface velocity information based on altimetry observations (Dibarboure *et al.* 2025). However, methodologies for deriving surface velocities from sea surface height using SWOT observations are still under development and not yet fully operational, particularly for the MIZ.

Analysis of remote sensing sea ice imagery has been proposed as a unique alternative to standard techniques for the characterisation of the turbulent eddy field in MIZ, albeit qualitatively. The first description of subsurface ocean eddies imprinted on ice edges in the Fram Strait MIZ was made using airborne remote sensing imagery (Johannessen *et al.* 1987). More recently, studies employing synthetic aperture radar (SAR) images have detected the distinct signature of ocean eddies and filaments on the distribution of sea ice, enabling the quantification of eddy counts, sizes and positions (Kozlov *et al.* 2019; Cassianides *et al.* 2021; Kozlov & Atadzhanova 2022). Similarly, under-ice

eddy characteristics have been inferred through Lagrangian observations of ice floe rotation rates (Manucharyan *et al.* 2022), retrieved from Moderate Resolution Imaging Spectroradiometer (MODIS) optical imagery (Lopez-Acosta, Schodlok & Wilhelmus 2019). This study demonstrated that upper-ocean eddy vorticity has a close relationship to ice floe rotations via ice–ocean torques, as atmospheric winds primarily drive ice floe advection, resulting in persistent daily-scale floe rotations.

From a fundamental standpoint, fluid flows have long been characterised in laboratory settings using micro-size particles as tracers. Inertialess spherical particles, for instance, serve as idealised passive tracers, effectively measuring flow fields via particle image velocimetry (Adrian & Westerweel 2011). However, different particle properties (e.g. inertia, shape, size) result in distinct behaviours. Particle inertia causes a delayed response to changes in the flow fields, leading to misalignment between particle motion and the background flow field (Mortensen *et al.* 2007; Ouellette, O'Malley & Gollub 2008; Zhao *et al.* 2015; Brandt & Coletti 2022). In turbulent shear flows, particle inertia can enhance rotational motion, especially near walls (Mortensen *et al.* 2007). Ouellette *et al.* (2008) also demonstrated that Lagrangian measurements of inertial particles along their trajectories differ from those of passive tracers in chaotic flows. In addition, inertial particles with different sizes and shapes exhibit unique rotational behaviours induced by local velocity gradients in various types of turbulent flows (Voth & Soldati 2017; Brandt & Coletti 2022), including homogeneous isotropic turbulence (Bordoloi & Variano 2017; Allende & Bec 2023), turbulent channel flow (Zhao *et al.* 2015) and turbulent boundary layers (Tee & Longmire 2024). These cumulative findings not only advance our fundamental understanding of particle dynamics but also suggest a promising potential for using particles to characterise a wide range of flow fields.

In systems where only a limited number of seeded particles are accessible, Lagrangian approaches using these particles provide an effective way of retrieving flow structure, and examples span cryogenic (Švančara *et al.* 2020) and environmental flows (Dauxois *et al.* 2021). For instance, in flows involving superfluid ^{4}He, where only 100 particles can be detected within a 1 Mpixel image, Outrata *et al.* (2021) employed Lagrangian particles to determine the vorticity of vortex rings. Similarly, in MIZ, Lagrangian tracking of ice floes presents a valuable opportunity to quantify ocean field characteristics. In general, during winter, when sea ice concentrations are high, eddy activity in the surface layer is weak, with only a limited number of eddies (Zhao *et al.* 2014). However, in MIZ observed during summer, where many ice floes are present, the eddy field at the surface layer is more active (Kozlov *et al.* 2019; Kubryakov *et al.* 2021; Kozlov & Atadzhanova 2022), suggesting that Lagrangian observations of ice floes may be useful for characterising underlying eddies. Recent efforts have also been aimed at characterising coherent structures and even flow fields using sparse trajectories of particles (Mowlavi *et al.* 2022; Harms, Brunton & McKeon 2024) and ice floes (Covington, Chen & Wilhelmus 2022). These cumulative findings in fluid mechanics with particles imply the potential of particle tracking to measure fluid vorticity, suggesting that sea ice could serve as an effective tracer for quantifying ocean flow fields.

In this study, we explore the kinematic relationship between ice floes and underlying ocean eddies, focusing specifically on the role of ice floe size relative to eddy size. We employ ocean eddy models (Arbic *et al.* 2012) and ice floe models (Manucharyan & Montemuro 2022; Montemuro & Manucharyan 2023) for ice floe–ocean simulations. Ice floe rotation in an idealised ocean vortex is examined, and analytical relations for ice floe rotation are introduced in § 3.2. The potential applicability of these analyses to more realistic ocean conditions is also discussed in § 3.3. The effects of key factors, such

Parameter	Symbol	Definition	Value
Amplitude of streamfunction (TG)	A_{TG}	—	1.23×10^3 m^{2}s^{-1}
Size of a vortex cell (TG)	L_{TG}	—	35 km
Domain size (QG)	L_{QG}	—	400 km
Rossby radius of deformation (QG)	L_d	—	5.2 km
Ratio of layer depths (QG)	δ	H_1/H_2	1
Vertical shear of horizontal currents (QG)	ΔU	$U_1 - U_2$	0.21 m s^{-1}
Effective drag length scale (QG)	r_1	$C_{d,eff}/H_1$	2×10^5 m^{-1}
Linear dissipation time scale (QG)	r_2	—	0.01 days^{-1}
Density (ocean)	ρ_o	—	1027 kg m^{-3}
Density (ice floe)	ρ_f	—	920 kg m^{-3}
Density (atmosphere)	ρ_a	—	1.2 kg m^{-3}
Sea ice–ocean drag coefficient	$C_{d,o}$	—	5.5×10^{-3}
Sea ice–atmosphere drag coefficient	$C_{d,a}$	—	1.0×10^{-3}
Turning angle (ocean)	θ_o	—	15°
Turning angle (atmosphere)	θ_a	—	0°
Radius (ice floe)	R_f	—	1–35 km
Thickness (ice floe)	h_f	—	0.1–1.0 m
Young's modulus (floe collisions)	E_f	—	5×10^7 Pa
Shear modulus (floe collisions)	G_f	$E_f/2(1+\nu)$	1.9×10^7 Pa
Poisson's ratio (floe collisions)	ν	—	0.3
Speed (atmosphere)	$\lvert\mathbf{u}_a\rvert$	—	0–12 m s^{-1}
Coriolis parameter	f	—	10^{-4} rad s^{-1}
Non-dimensionalised floe inertia	$H^*_{f,o}$	$\rho_f h_f/\rho_o C_{d,o} L_o$	10^{-3}–10^{-2}
Rossby number	Ro	$U_o/f L_o$	0.045
Nansen number	Na	$\sqrt{\rho_a C_{d,a}/\rho_o C_{d,o}}$	0.015

Table 1. Parameters and properties for ocean eddy (top) and ice floe (bottom) models.

as ice floe thickness (§ 4.1), atmospheric winds (§ 4.2), floe–floe collisions and sea ice concentration (§ 4.3), on the rotational relationship are examined in § 4.

2. Methods

2.1. *Ocean eddy models*

Two numerical models were employed to generate idealised ocean flow fields: (*a*) the Taylor–Green (TG) vortex and (*b*) a two-layer quasi-geostrophic (QG) model. We describe the key details of the TG and QG simulations in turn. Simulation parameters for the two models are summarised in table 1.

The TG vortex is an idealised two-dimensional flow field frequently employed in the literature due to its exact closed-form solutions for incompressible flows. For example, it has been used as a background flow field in studies of multiphase flows to investigate the motion of particles (Wereley & Lueptow 1999; Qiao, Deng & Wang 2015; Jayaram *et al.* 2020), bubbles (Deng, Wang & Smith 2006) and droplets (Qiao, Deng & Wang 2014) in idealised flow settings. Here, we examine the motion of ice floes over a TG vortex and derive analytical expressions for their relationship.

We consider a TG vortex cell of size L_{TG} centred at the origin, defined by $|x|, |y| \leqslant 0.5L_{TG}$. The streamfunction of the square-shaped TG vortex is given by

$$\psi_{TG} = -A_{TG}\cos\left(\frac{\pi x}{L_{TG}}\right)\cos\left(\frac{\pi y}{L_{TG}}\right), \tag{2.1}$$

where A_{TG} is the amplitude, and x and y are the spatial coordinates. Maximum vorticity magnitude occurs at the vortex centre, gradually decreasing radially outward until reaching zero at the boundary of the vortex cell. Without loss of generality, we consider only the cyclonic case. Both anticyclonic and cyclonic eddies are present in the Arctic Ocean, yet for the results derived here, the anticyclonic and cyclonic cases differ only in sign.

The two-layer QG model produces more realistic ocean eddies similar in size and shape to those observed in the MIZ. We employed the QG flow field tuned to observations from the Beaufort Gyre (BG) (Manucharyan *et al.* 2022). Full details of the model and the tuning of its parameters can be found in Arbic *et al.* (2012) and Manucharyan *et al.* (2022). The QG model set-up divides the ocean into two vertical layers. The model is forced by an imposed mean flow assumed to be homogeneous in the horizontal direction. The vertically sheared horizontal flows in these two layers induce a baroclinic instability, resulting in the generation of eddies evolving over the horizontal plane of each layer, which is the most common eddy generation mechanism in the global ocean (Tulloch *et al.* 2011), including the Arctic BG (Hunkins 1974; Manucharyan & Stewart 2022). In both layers, the mean horizontal velocity is imposed in the zonal direction U, leading to gradients in the mean potential vorticity, Q, which accounts for vorticity with the presence of stratification. These velocity and vorticity gradients result in zonal (x) and meridional (y) velocity perturbations (u and v) as well as potential vorticity perturbation (q). The evolution of the perturbation vorticity fields in each layer is described by the QG equations, which account for the Coriolis force and the vertical shear of the velocity. There is no internal friction between layers. The governing equations for each layer are as follows:

$$\frac{\partial q_1}{\partial t} + (u_1 + U_1)\frac{\partial q_1}{\partial x} + v_1\frac{\partial q_1}{\partial y} = -v_1\frac{\partial Q_1}{\partial y} - r_1|\nabla \times \mathbf{u}_1||\mathbf{u}_1| + s.s.d., \tag{2.2}$$

$$\frac{\partial q_2}{\partial t} + (u_2 + U_2)\frac{\partial q_2}{\partial x} + v_2\frac{\partial q_2}{\partial y} = -v_2\frac{\partial Q_2}{\partial y} - r_2\nabla^2\psi_2 + s.s.d., \tag{2.3}$$

where subscripts 1 and 2 denote the top and bottom layers, respectively, t is the time, $\mathbf{u}$ is the vector form of the perturbed velocity, $r_1 = C_{d,eff}/H_1$ stands for the effective drag length scale for the top layer, $C_{d,eff}$ is the effective sea ice-ocean drag coefficient, H is the layer depth, r_2 is the linear dissipation time scale for the bottom layer, ψ is the perturbation streamfunction and $s.s.d.$ is small-scale dissipation using an exponential cutoff filter. In this set of equations, uniform dissipation caused by the quadratic sea ice–ocean drag is incorporated in the entire horizontal domain of the top layer, while Ekman-type friction is included in the bottom layer. Small-scale dissipation is also considered to prevent a forward-enstrophy cascade towards small scales. The imposed mean potential vorticity gradients are given by

$$\frac{\partial Q_1}{\partial y} = \frac{U_1 - U_2}{(1+\delta)L_d^2}, \qquad \frac{\partial Q_2}{\partial y} = \frac{\delta\,(U_2 - U_1)}{(1+\delta)L_d^2}, \tag{2.4}$$

where $\delta = H_1/H_2$ is the ratio of layer depths, L_d is the Rossby radius of deformation and $\Delta U = U_1 - U_2$ is the vertical shear of horizontal currents. The perturbation potential vorticities in the two layers are given by

$$q_1 = \nabla^2\psi_1 + \frac{\psi_2 - \psi_1}{(1+\delta)L_d^2}, \qquad q_2 = \nabla^2\psi_2 + \frac{\delta(\psi_1 - \psi_2)}{(1+\delta)L_d^2}. \tag{2.5}$$

The model uses an f-plane approximation since the Coriolis parameter is approximately constant in the Arctic Ocean (Timmermans & Marshall 2020).

The simulation domain spans 400 km × 400 km and is set up with doubly periodic boundary conditions. Time integration was performed using the Adams–Bashforth two-step method in Fourier space with 256 modes, producing a converged energy spectrum previously validated by Manucharyan *et al.* (2022). The model was initialised with randomly generated q_1 and q_2 in Fourier space. The simulation was conducted until the flow field reached an equilibrated state. At that point, the energy production from the mean flow was balanced by the energy dissipation from the top and bottom layers due to the sea ice–ocean drag and the Ekman drag, respectively. This equilibration state is typically achieved after approximately one simulation year. The model tuning parameters, L_d, δ and ΔU, were adopted from Manucharyan *et al.* (2022). As a result, the simulated eddy fields closely matched the statistics of the BG MIZ between 2003 and 2020. It is important to note that the sizes of the produced eddies are within the observed range of the eddy sizes (of the order of 10 km) in the MIZ (Johannessen *et al.* 1987; Kozlov *et al.* 2019; Kozlov & Atadzhanova 2022). In addition, the estimated eddy kinetic energy derived from the simulated ice floes is comparable to the estimated eddy kinetic energy from *in situ* measurements via moorings located in the area of the satellite observations (Manucharyan *et al.* 2022).

Arctic MIZ eddies typically persist for a period of $O(10)$ days (Johannessen *et al.* 1987; Kozlov, Plotnikov & Manucharyan 2020; Cassianides *et al.* 2021; Kozlov & Atadzhanova 2022); hence, we consider stationary ocean fields during the 30 day simulation period. Note that the simulation incorporates the effects of sea ice–ocean drag as an effective, continuous, stationary drag force over the top layer, influencing the energetics of the QG eddy field. The quadratic drag law is used due to the turbulent nature of the flow field, consistent with studies on the ice–ocean boundary layer (McPhee 2012; Cole *et al.* 2014). The effective sea ice–ocean drag coefficient represents the overall impact of drag forces on the ocean field, implying the product of sea ice concentration and the actual ice–ocean drag coefficient (Manucharyan & Stewart 2022). This constant coefficient neglects the small-scale floe dynamics and seasonal variations. For the given Rossby radius, changes in the effective drag coefficient of less than 25% compared with the tuned value have negligible effects on the slope of the eddy energy spectrum. This implies that such variations in ice floe surface properties may have a limited impact on energy transport across scales.

While the tuning parameters in the QG model can produce consistent eddy energetics, local eddy sizes and velocities may vary, even for simulation runs set up with identical tuning parameters. Therefore, instead of covering a wide range of eddy sizes, we set the parameters in the TG vortex model according to the relative length scales of eddies and ice floes (table 1). The majority of the observed ice floe sizes range from 1 to 35 km (Manucharyan *et al.* 2022). The value of L_{TG} was set to broadly cover the floe–eddy size ratios from 0.05 to 2. Ratios higher than 2 were excluded, as these larger floes tend to filter out most of the eddy information and have a limited reflection of the local eddies underneath them. Concurrently, A_{TG} in (2.1), was chosen to represent the maximum velocity of local QG eddies corresponding to L_{TG}. These length and velocity scales fall within the ranges of observed eddy sizes (1–40 km) (Kozlov *et al.* 2019) and flow speeds (0–0.5 m s^{-1}) (Kozlov & Atadzhanova 2022) in the BG MIZ.

Finally, local eddies (or coherent vortices) in ocean flow fields are identified in this study by using the Lagrangian-averaged vorticity deviation (LAVD)-based approach proposed by Haller *et al.* (2016). We note that other identification schemes exist, such as the Okubo–Weiss parameter (Okubo 1970; Isern-Fontanet *et al.* 2004), Lagrangian trajectory methods (Haller 2005; Dong *et al.* 2011) and others based on the values of sea surface heights and vorticity (Chelton, Schlax & Samelson 2011; Mason, Pascual & McWilliams 2014). We opted for the LAVD-based eddy detection method given that it is both time

and rotation invariant and has demonstrated good performance in detecting coherent structures in altimeter-derived velocity fields of the global ocean (Archiving, Validation and Interpretation of Satellite Oceanographic (AVISO) data) (Abernathey & Haller 2018; Liu & Abernathey 2023). More details are provided in § 3.3.

2.2. *Sea ice model*

We simulate the motion of circular ice floes using the SubZero discrete element sea ice model (Manucharyan & Montemuro 2022). This model is designed to study the behaviour of ice floes under mechanical forcing. We parameterise the sea ice–ocean and sea ice–atmosphere stresses through a quadratic drag law (Leppäranta 2011)

$$\boldsymbol{\tau}_o = \rho_o C_{d,o} |\mathbf{u}_o - \mathbf{u}_i| e^{i\theta_o} (\mathbf{u}_o - \mathbf{u}_i), \quad \boldsymbol{\tau}_a = \rho_a C_{d,a} |\mathbf{u}_a - \mathbf{u}_i| e^{i\theta_a} (\mathbf{u}_a - \mathbf{u}_i), \tag{2.6}$$

where $\boldsymbol{\tau}$ is the shear stress, ρ is the density, θ is the turning angle and the subscripts o, a and i correspond to the ocean, the atmosphere and the ice floe, respectively. Since $\mathbf{u}_a \gg \mathbf{u}_i$, $(\mathbf{u}_a - \mathbf{u}_i) \approx \mathbf{u}_a$ was used. The ocean turning angle is the angle between the geostrophic current and the surface shear stress, as the Coriolis effect causes the flow to turn within the boundary layers. Here, $\mathbf{u}_o$ represents the velocity of the geostrophic current beneath the Ekman layer (∼20 m (Yang 2006; Ma, Steele & Lee 2017)), with a direction rotated relative to the ocean surface velocity by a turning angle of θ_o. The geostrophic velocity generally has larger magnitudes than the surface ocean velocity in the BG due to sea ice–ocean drag. The wind turning angle is set to zero, as the surface wind is considered.

The velocity of ice floes comprises translational and rotational components, $\mathbf{u}_i = \mathbf{u}_f + \Omega_f \hat{\mathbf{k}} \times \mathbf{r}'$, where $\mathbf{u}_i$ is the sea ice velocity over the ice floe area, $\mathbf{u}_f$ is the translational velocity of the centre of mass, Ω_f is the rotation rate of the ice floe and $\mathbf{r}' = \mathbf{r} - \mathbf{r}_C$ is the position vector on the ice floe with respect to its centre of mass, C. The translational velocity and rotation rate of ice floes evolve according to the linear and angular momentum conservation equations

$$M_f \left(\frac{\mathrm{d}\mathbf{u}_f}{\mathrm{d}t} + f\hat{\mathbf{k}} \times \mathbf{u}_f \right) = \iint_A \left(\boldsymbol{\tau}_o + \boldsymbol{\tau}_a - \rho_f h_f g \nabla \eta \right) \mathrm{d}A + \sum_{j,k} \mathbf{F}_{j,k}, \tag{2.7}$$

$$I_f \frac{\mathrm{d}\Omega_f}{\mathrm{d}t} = \iint_A \mathbf{r}' \times \left(\boldsymbol{\tau}_o + \boldsymbol{\tau}_a - \rho_f h_f g \nabla \eta \right) \mathrm{d}A + \sum_{j,k} \mathbf{r}'_{j,k} \times \mathbf{F}_{j,k}, \tag{2.8}$$

where $M_f = \rho_f A_f h_f$ is the floe mass, ρ_f is the floe density, $A_f = \pi R_f^2$ is the floe area, h_f is the floe thickness, R_f is the floe radius, t is time, g is the gravitational acceleration, η is the sea surface height anomaly associated with ocean currents, A is the surface area covered by an ice floe, $\mathbf{F}_{j,k}$ is the interaction forces of the kth contact point with the jth ice floe due to collisions, $I_f = M_f R_f^2/2$ is the moment of inertia for a floe with an axis passing through the centre of mass and $\mathbf{r}'_{j,k} = \mathbf{r}_{j,k} - \mathbf{r}_C$ is the position vector on the kth contact point with the jth ice floe with respect to its centre of mass. The left-hand side of (2.7) represents the rate of change of ice floe momentum and the Coriolis force acting on ice floes, while the integration terms on the right-hand side consist of the sea ice–ocean stress, the sea ice–atmosphere stress and the pressure gradient due to the sea surface tilt. Equation (2.8) consists of the corresponding torque terms. Floe–floe collisions are neglected for ice floes subjected only to oceanic and wind forcings, resulting in $\mathbf{F}_{j,k} = 0$. While these floes can be more observable in regions with low sea ice concentrations, they effectively capture the key connections between ice floes and underlying eddies. In addition, it establishes a

baseline for ice floe motions in regions with high concentrations. Free-drifting ice floes with no collisions are examined in most sections, while the effects of floe–floe collisions are discussed in § 4.3.

Using the length L_o, velocity U_o and time T_o scales of the ocean field, (2.7) and (2.8) can be rewritten in non-dimensionalised form

$$\frac{\mathrm{d}\mathbf{u}_f^*}{\mathrm{d}t^*} = \frac{1}{H_{f,o}^*}\iint_{A^*} |\mathbf{u}_o^* - \mathbf{u}_i^*| e^{i\theta_o}\left(\mathbf{u}_o^* - \mathbf{u}_i^*\right)\mathrm{d}A^* + \frac{Na^2}{H_{f,o}^*}\iint_{A^*} |\mathbf{u}_a^* - \mathbf{u}_i^*|\left(\mathbf{u}_a^* - \mathbf{u}_i^*\right)\mathrm{d}A^* + \frac{1}{Ro}\iint_{A^*} \hat{\mathbf{k}} \times (\mathbf{u}_o^* - \mathbf{u}_f^*)\mathrm{d}A^*, \tag{2.9}$$

$$\frac{\mathrm{d}\Omega_f^*}{\mathrm{d}t^*} = \frac{2}{R_f^{*2}}\left[\frac{1}{H_{f,o}^*}\iint_{A^*} \mathbf{r}'^* \times \left[|\mathbf{u}_o^* - \mathbf{u}_i^*| e^{i\theta_o}\left(\mathbf{u}_o^* - \mathbf{u}_i^*\right)\right]\mathrm{d}A^* + \frac{Na^2}{H_{f,o}^*}\iint_{A^*} \mathbf{r}'^* \times \left[|\mathbf{u}_a^* - \mathbf{u}_i^*|\left(\mathbf{u}_a^* - \mathbf{u}_i^*\right)\right]\mathrm{d}A^* + \frac{1}{Ro}\iint_{A^*} \mathbf{r}'^* \times \left(\hat{\mathbf{k}} \times \mathbf{u}_o^*\right)\mathrm{d}A^*\right], \tag{2.10}$$

where $H_{f,o}^* = \rho_f h_f / \rho_o C_{d,o} L_o$ is the non-dimensionalised floe inertia characterising ice floe inertia relative to surface ocean drag, $Na = \sqrt{\rho_a C_{d,a}/\rho_o C_{d,o}}$ denotes the Nansen number, $Ro = U_o/fL_o$ denotes the Rossby number, $A^* = A/A_f$ is the non-dimensionalised floe area and the superscript $*$ indicates non-dimensionalised quantities. Note that the sea surface height tilt terms in (2.7) and (2.8) are rewritten using $-g\nabla\eta = f\hat{\mathbf{k}} \times \mathbf{u_o}$, indicating the geostrophic balance between the pressure gradient force due to the sea surface tilt and the Coriolis force. Interaction forces due to floe–floe collisions are neglected in the non-dimensionalised forms.

Simulations with the SubZero model employ an Adams–Bashforth two-step method for time integration and a Monte Carlo scheme (Caflisch 1998) at each time step for spatial integration of forces and torques acting on individual ice floes. The velocity and rotation rate of ice floes are initialised with the averaged values of ocean eddies beneath them. In this study, we excluded the first five days of simulation to eliminate any influence of initial conditions on the dynamics. An extensive description of the Subzero model can be found in Manucharyan & Montemuro (2022) and Montemuro & Manucharyan (2023). The codes associated with the model are available at https://github.com/SeaIce-Math/SubZero.

The physical properties of the ocean, sea ice and the atmosphere used in the simulations are chosen based on geostrophic drag coefficients and turning angles specific to conditions in the BG MIZ (table 1, from Leppäranta (2011) and Brenner *et al.* (2021)). We considered ice floes with sizes ranging from 1 to 35 km, covering most of the observations acquired in the BG MIZ from 2003 to 2020 (Manucharyan *et al.* 2022). We removed the influence of shape variations on the rotational relationship between ice floes and the ocean by reducing observed floe geometries to circular shapes. This agrees with studies by Gupta & Thompson (2022) and Gupta, Gürcan & Thompson (2024). For non-dimensionalisation, the size and the velocity amplitude of a TG vortex are taken as the reference length and velocity scales, respectively.

For the initial part of this study, we considered ice floes with a constant thickness of $h_f = 0.5$ m, in agreement with observed values in the BG MIZ (Krishfield *et al.* 2014; Timmermans & Marshall 2020; Manucharyan *et al.* 2022). We also neglected atmospheric stresses. The effects of varying ice floe thickness and wind speeds on the rotational relationship between ice floes and underlying ocean eddies are presented in §§ 4.1 and 4.2.

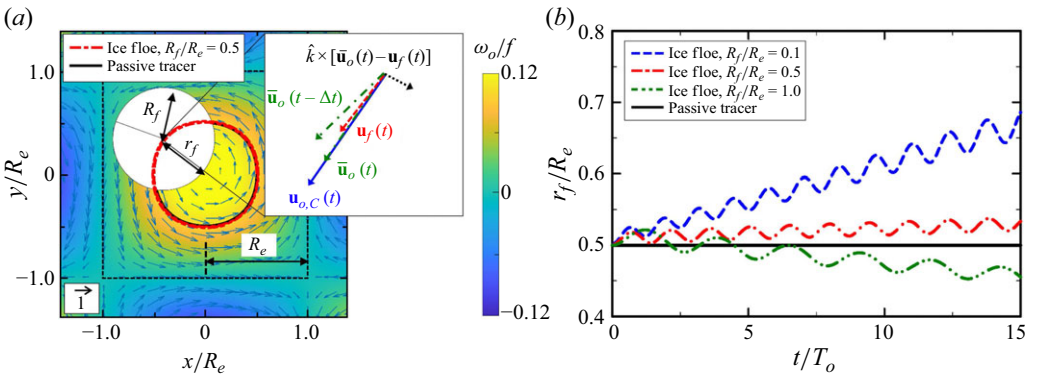

Figure 1. Ice floes drifting over a TG vortex field. (*a*) The trajectory of a circular ice floe released at the radial position, r_f, set to be half of the TG vortex size, R_e ($R_f/R_e = 0.5$). The colours map the magnitude of the fluid vorticity normalised by the Coriolis parameter, while the arrows indicate the direction of the fluid velocity (with the arrow size set to scale according to the velocity magnitude) at a given location. The inset schematic shows the orientation of relevant vectors: the ocean velocity averaged over the floe area, $\overline{\mathbf{u}}_o$, the ocean velocity at the centre of mass of the floe, $\mathbf{u}_{o,C}$, the ice floe velocity at its centre of mass, $\mathbf{u}_f$ and the force direction resulting from combining the Coriolis force and the pressure gradient force due to the sea surface tilt, $\hat{k}\times(\overline{\mathbf{u}}_o - \mathbf{u}_f)$. (*b*) Radial positions of ice floes with floe–eddy size ratios of $R_f/R_e = 0.1$ (blue dashed lines), 0.5 (red dot-dashed lines) and 1.0 (green double dot-dashed lines), normalised by the size of the eddy. The ice floe cases are compared with the passive tracer case (black solid lines). Supplementary movies are available at https://doi.org/10.1017/jfm.2025.10213.

Lastly, the passive tracer, devoid of inertia, perfectly follows the fluid, mirroring the local velocity and rotation of fluid flows. The passive tracer scenario serves as an idealised baseline case in our analysis.

3. Results

This section investigates the rotational relationship between ice floes and underlying ocean eddies for different floe–eddy size ratios in the TG vortex and two-layer QG flow fields. Two types of ocean quantities were explored for the analyses: (i) area-averaged ocean quantities, calculated by averaging ocean quantities over the ice floe area, representing localised ocean information in regions with ice floe coverage and (ii) centre-of-mass ocean quantities, obtained through the interpolation of quantities at the centre of mass of the ice floe, offering pointwise ocean information. These two types of quantities are complementary; area-averaged quantities can be used to create spatial vorticity maps when sea ice concentration is high, while quantities derived from information at the centre of mass can be leveraged to estimate ocean vorticity at lower concentrations, mainly when ice floes undergo a closed-loop trajectory over a larger area.

3.1. *Single ice floe dynamics*

The motion of individual ice floes with different sizes was analysed in a TG vortex field and compared with the passive tracer case (figure 1). Three floe–eddy size ratios were considered, $R_f/R_e = 0.1$, 0.5 and 1.0. In all cases, the centre of mass of the ice floes was initially positioned at $r_f = 0.5R_e$, where r_f denotes the radial position of the floe centre of mass, to capture the influence of ocean fields both inside and outside the vortex cell.

The trajectories of free-drifting ice floes are shaped by oceanic and atmospheric forcing, the effects of floe inertia, the Coriolis force and the pressure gradient force due to the sea surface tilt. Under low to negligible wind speeds and low sea ice concentration, ice

floe motion is expected to be predominantly driven by oceanic forcing. However, it has been hypothesised that ice floe inertia plays an important role in setting the direction in which floes translate by delaying their response to changes in the underlying ocean flow field. From the cases tested, the ice floe with a size ratio of $R_f/R_e = 0.5$ exhibited the best performance at resembling a passive tracer and forming a closed-loop trajectory over the TG vortex cell (figure 1*a*). While inertia does result in an outward tilt of the ice floe velocity $\mathbf{u}_f(t)$ relative to the ocean velocity averaged over the floe area at t, $\overline{\mathbf{u}}_o(t)$ (a subset of figure 1*a*), the resulting force from combining the Coriolis force and the pressure gradient force due to the sea surface tilt, $\hat{k} \times (\overline{\mathbf{u}}_o - \mathbf{u}_f)$, reduces this spiralling effect, effectively driving the ice floe to form a closed loop (figure 1*a*). Finally, ice floes were observed to undergo alternating periods of acceleration and deceleration relative to the equilibrium state in which all forces balance instantaneously to zero. As a result, the radial component of floe position oscillates (figure 1*b*).

Changes in floe size with respect to vortex size result in a deviation of floe motion with respect to the eddying motion underneath. For example, smaller ice floes, for which $R_f/R_e = 0.1$, followed an outwardly spiral trajectory. In this case, the ice floe velocity and the averaged ocean velocity vectors were better aligned, reducing the inward effect from the Coriolis and pressure gradient forces compared with floes with larger size ratios. This is similar to the behaviour of millimetre-sized particles in a Taylor vortex (Wereley & Lueptow 1999; Deng *et al.* 2006; Qiao *et al.* 2015) and a Rankine vortex (Varaksin & Ryzhkov 2022), in which the role of inertia is linked to their resulting spiral trajectories relative to the flow direction. As the floe–eddy size ratio increases to $R_f/R_e = 1.0$, discrepancies between ice floe and averaged ocean velocities become more pronounced due to filtration of measured ocean velocities over larger floe areas. This results in larger forces directed toward the vortex centre compared with smaller floes, leading to an inward spiralling motion.

The kinematics of ice floes with different sizes were examined along their trajectories (figure 2). We present results using two normalisations: (i) considering ocean quantities averaged over the floe area, including averaged ocean vorticity, $\overline{\omega}_o$, and averaged ocean speed, $\overline{V}_o$ and (ii) ocean quantities at the floe centre of mass, such as ocean vorticity, $\omega_{o,C}$, and ocean speed, $V_{o,C}$. Note that the floe rotation rates are normalised by half of the ocean vorticity. Angle deviations are calculated by subtracting the angle of the ocean velocity from that of the ice floe velocity, $\Delta\theta_f = \theta_f - \overline{\theta}_o$ and $\Delta\theta_{f,C} = \theta_f - \theta_{o,C}$, where θ_f denotes the angle of the ice floe velocity, $\overline{\theta}_o$ denotes the angle of the ocean velocity averaged over the ice floe area and $\theta_{o,C}$ denotes the angle of the ocean velocity at the centre of mass of the ice floe. All angles are calculated using the direction of each velocity vector with respect to the positive x-axis, measured in the counter-clockwise direction.

Normalised ice floe rotation rates, velocities and orientations oscillated over time, periodically crossing the equilibrium values. Small ice floes with $R_f/R_e = 0.1$ show higher sensitivity to local ocean quantities, leading to normalised rotation rates and speeds close to unity and minimal angle deviations (figure 2). Ocean quantities averaged over the floe area and at the floe centre of mass exhibit similar values, resulting in comparable normalised rotation rates (figures 2*a* and 2*b*) and speeds (figures 2*c* and 2*d*). As ice floes move farther from the vortex centre along their outwardly spiral trajectories, the normalised rotation rates begin to decrease at later times. The angle deviations have negative values for most of the evolution time due to the outwardly spiral shape of the trajectory (figures 2*e* and 2*f*). Contrasting the ice floe case, the passive tracer perfectly mirrors the vorticity and velocity of the underlying flow field with zero angle deviations.

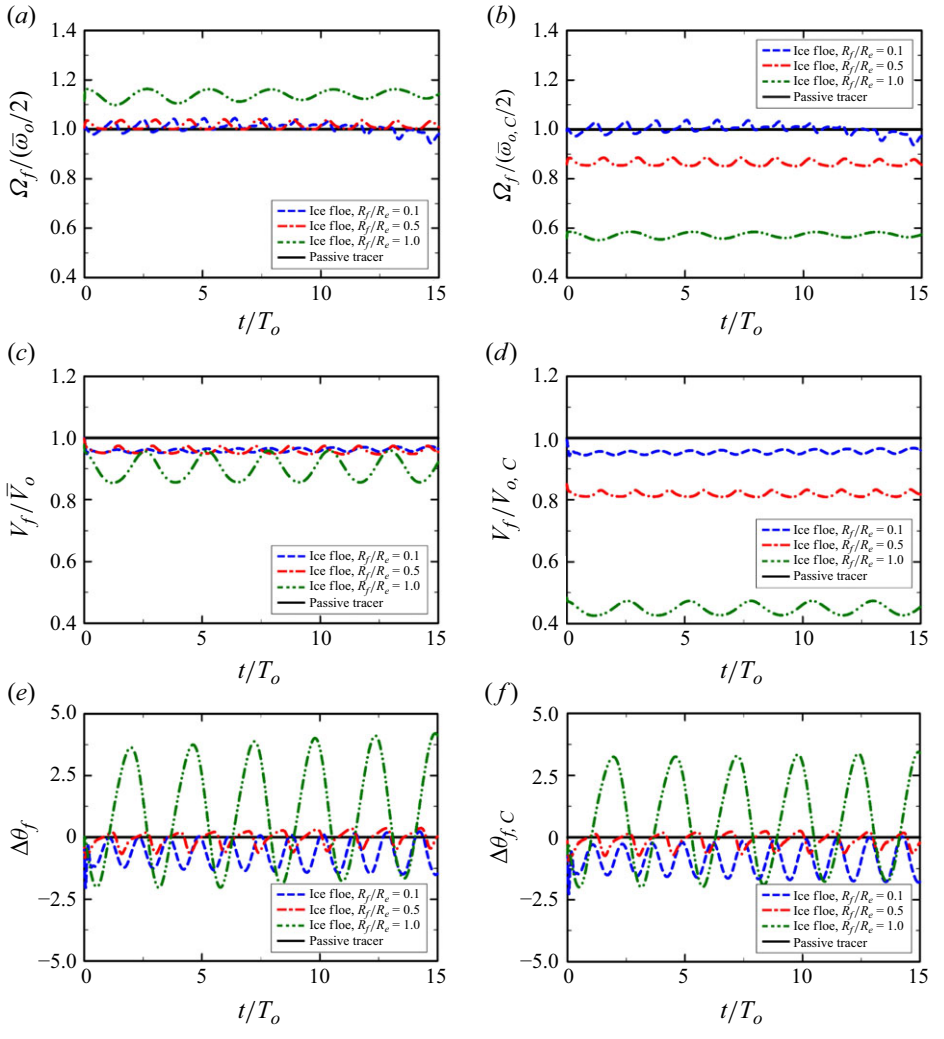

Figure 2. Motions of ice floes with different sizes in a TG vortex field. (a, b) Normalised rotation rates, Ω_f, (c, d) speeds, V_f and (e, f) angle deviations of ice floes for floe–eddy size ratios of $R_f/R_e = 0.1$ (blue dashed lines), 0.5 (red dot-dashed lines) and 1.0 (green double dot-dashed lines) are compared with the passive tracer case (black solid lines). Floe rotation rates are normalised by the (a) ocean vorticity averaged over the floe area, $\overline{\omega}_o$, and (b) ocean vorticity at the floe centre of mass, $\omega_{o,C}$. Floe speeds are normalised by (c) ocean speed averaged over the floe area, $\overline{V}_o$, and (d) ocean speed at the floe centre of mass, $V_{o,C}$. Angle deviations are calculated by subtracting the angle of the (e) averaged ocean velocity, $\Delta\theta_f$, and the (f) centre-of-mass ocean velocity, $\Delta\theta_{f,C}$, from that of the ice floe velocity. The ice floes are initially released at $r_f/R_e = 0.5$.

As the floe–eddy size ratios increase to $R_f/R_e = 1.0$, the normalised ice floe rotation rates and speeds exhibit larger deviations from unity (figure 2a–d). With larger floe–eddy size ratios, the floe rotation rates normalised by the averaged ocean vorticity increase because the floe samples low-vorticity regions near cell boundaries, reducing the averaged ocean vorticity (figure 2a). Conversely, the floe speeds normalised by the averaged ocean speed decrease due to high-velocity regions near the cell boundaries covered by the floe area, resulting in higher averaged ocean speed (figure 2c). In the context of ocean quantities at the floe centre of mass, the normalised rotation rates and speeds of ice floes decrease significantly for larger floe–eddy size ratios. This occurs because the ocean vorticity and

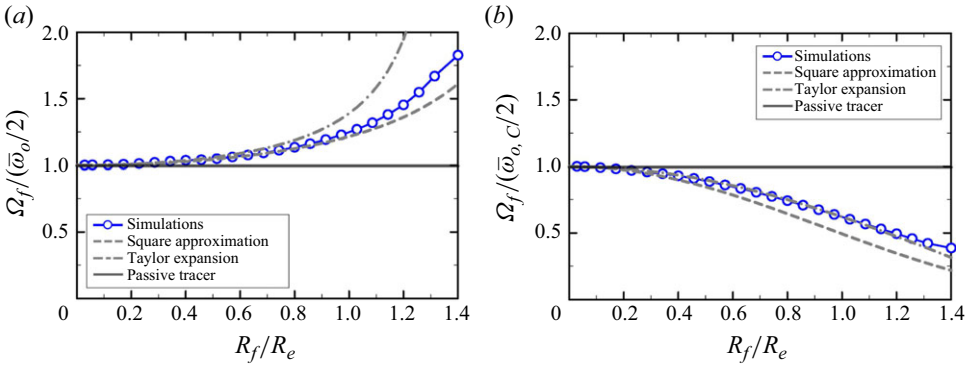

Figure 3. Rotational motion of centred ice floes in a TG vortex field. Ice floe rotation rates, Ω_f, normalised by the (*a*) ocean vorticity averaged over the floe area, $\overline{\omega}_o$, and the (*b*) the ocean vorticity at the floe centre of mass, $\omega_{o,C}$, for different floe–eddy size ratios, R_f/R_e. The simulation results are compared with analytical relations using square-shape approximation (dashed lines) and Taylor series expansion (dashed-dotted lines), and the passive tracer case (solid lines).

velocity at the floe centre of mass are considerably higher compared with the values averaged over the floe area (figures 2*b* and 2*d*). For both types of ocean quantities, the angle deviation becomes more pronounced as the floe–eddy size ratios increase (figures 2*e* and 2*f*). With larger ratios, the resultant forces from a combination of the Coriolis force and the pressure gradient force due to the sea surface tilt become larger, resulting in a shift of floe trajectories from an outwardly spiral shape to an inwardly spiral shape as the ratios increase. As a result, the angle deviations at $R_f/R_e = 0.5$ are smaller than in the other two cases since the floe trajectories form nearly closed loops. Floes with $R_f/R_e = 1.0$ show positive angle deviations since they have inwardly spiralling trajectories.

The motion of a single floe provides insight into the instantaneous response of ice floes to an underlying ocean eddy flow field. Our results demonstrate the importance of floe–eddy size ratios modulating the distribution of forces due to drag, Coriolis and the pressure gradient on ice floes as they drift over ocean eddy fields.

3.2. *Statistics of ice floe kinematics in an idealised vortex*

Based on the statistics of ice floes in a TG vortex field, we derived analytical expressions describing the kinematic link between ice floe rotation and the ocean vorticity underneath. Appendix A outlines the criteria for identifying trapped ice floes. Given the time duration of the simulation and the requirements for floe selection, ice floes with floe–eddy size ratios ranging from 0.05 to 1.4 were considered for further analysis.

We examined ice floes positioned at the centre of a TG vortex representing an idealised scenario (figure 3). In this case, the ice floes are initially released at the centre of the vortex, exhibiting a distinct trend in their rotation driven solely by spatial variations in ocean vorticity within the vortex core. The ice floe rotation rate normalised by the ocean vorticity averaged over the floe area shows a monotonic growth with increasing floe–eddy size ratios (figure 3*a*). This observed rise in rotation rates can be attributed to the gradual decline in local ocean vorticity from the centre of a vortex cell toward its periphery. As floe–eddy size ratios increase, the averaged ocean vorticity decreases, increasing normalised rotation rates. In contrast, the rotation rate normalised by the ocean vorticity at the floe centre of mass decreases for larger floe–eddy size ratios (figure 3*b*). This is due to the fact that large ice floes rotate at slower rates while the ocean vorticity is maximised at the centre of mass of the rotating ice floes.

Building upon the physical interpretation of ice floe rotation, we established analytical relations for the normalised rotation rates by balancing the torques acting on the ice floes. In the present analysis, the quadratic drag terms in the angular momentum equation (2.10) are substituted with linear drag, thereby enabling the derivation of explicit relations describing the dependence of the normalised rotation rates on floe–eddy size ratios. We investigated the effect of this substituted parameterisation on the rotational relationship using the Rankine vortex, a simplified case for which solutions for both drag parameterisations can be derived. The analytical relation for the normalised rotation rate of ice floes shows minimal sensitivity to the choice of drag parametrisation, as detailed in Appendix B, such that a linear drag law was used in deriving an analytical relation.

By introducing a so-called size parameter, $\gamma = R_f/R_e$, we derived an analytical relationship for the normalised rotation rate of an ice floe located at the centre of the TG vortex. Near the centre of the TG vortex ($2\pi x/L_{TG}$, $2\pi y/L_{TG} \ll 1$), the ocean surface velocity can be approximated using a Taylor series expansion. In the absence of wind, ice floe rotation is dominated by ice–ocean stress for which the induced equilibrium of torques leads to the relation

$$\iint_{A^*} \mathbf{r}_f'^{*} \times (\mathbf{u}_f^* - \mathbf{u}_o^*) \mathrm{d}A^* = 0. \tag{3.1}$$

Substituting the second-order Taylor series expansion into (3.1) yields the following expression for the ice floe rotation rate normalised by the averaged ocean vorticity:

$$\frac{\Omega_f}{\overline{\omega}_o/2} = \frac{\left[1 - \dfrac{\pi^2}{8}\left(\dfrac{\gamma^2}{3}\right) + \dfrac{\pi^4}{64}\left(\dfrac{\gamma^4}{48}\right)\right]}{\left[1 - \dfrac{\pi^2}{8}\left(\dfrac{\gamma^2}{2}\right) + \dfrac{\pi^4}{64}\left(\dfrac{\gamma^4}{24}\right)\right]}. \tag{3.2}$$

Given that the ocean vorticity at the centre of mass of the centred floe in the TG vortex is $\omega_{o,C} = 2A\pi^2/L_{TG}^2$, the ice floe rotation rate normalised by the ocean vorticity at the floe centre of mass can be expressed as

$$\frac{\Omega_f}{\omega_{o,C}/2} = \left[1 - \frac{\pi^2}{8}\left(\frac{\gamma^2}{3}\right) + \frac{\pi^4}{64}\left(\frac{\gamma^4}{48}\right)\right]. \tag{3.3}$$

Equation (3.2) is in good agreement with the simulation results for the rotation rates normalised by the averaged ocean vorticity provided $R_f/R_e \leqslant 0.7$ (figure 3*a*). In this range, the Taylor series approximation effectively restores the original functions. However, we observed noticeable deviations in the normalised rotation rate when the ice floe size exceeded the eddy size due to limitations of the Taylor series expansion near the edge of the vortex cell. Equation (3.3) aligns well with simulation results for the rotation rate normalised by the ocean vorticity at the floe centre of mass for different floe–eddy size ratios because the ocean vorticity remains constant (figure 3*b*).

We derived another analytical relation for the normalised rotation rate of the centred ice floe by approximating the floe shape as a square with the same characteristic length scale. With the equilibrium condition for ice–ocean stress torques, the analytical relation can be expressed as

$$\frac{\Omega_f}{\overline{\omega}_o/2} = \frac{12}{\pi^2\gamma^2}\left[1 - \frac{\pi\gamma}{2}\cot\left(\frac{\pi\gamma}{2}\right)\right]. \tag{3.4}$$

We positioned square-shaped floes centred with respect to the origin. This simplification allows for the direct use of trigonometric functions. As a result, the ice floe rotation rate normalised by the ocean vorticity at the floe centre of mass can be written as

$$\frac{\Omega_f}{\omega_{o,C}/2} = \frac{12}{\pi^2\gamma^2}\left[\frac{\sin\left(\frac{\pi\gamma}{2}\right)}{\frac{\pi\gamma}{2}}\right]^2\left[1-\frac{\pi\gamma}{2}\cot\left(\frac{\pi\gamma}{2}\right)\right]. \tag{3.5}$$

Equation (3.4) closely matches the simulation results for the rotation rates normalised by the averaged ocean vorticity because it incorporates trigonometric functions fully in the solution (figure 3*a*). However, (3.5) deviates from the simulation results for the rotation rates normalised by the centre-of-mass ocean vorticity due to the square-shape approximation (figure 3*b*). It is worth noting that, for the centred ice floes, the derived analytical relations (3.2)–(3.5) are functions solely of the floe–eddy size ratios.

We also examined a more realistic scenario of an ice floe being positioned off centre with respect to the TG vortex cell. We conducted simulations with over 2000 randomly distributed ice floes for each floe–eddy size ratio. While centred ice floes remain at the vortex centre, off-centred ice floes have the potential to drift away, depending on their radial positions. For the present analysis, only trapped ice floes were considered.

The normalised rotation rates of off-centred floes are dependent on the position of the floes relative to the vortex core. Therefore, to analyse this case, we computed probability density functions (PDFs) over all floe positions for each bin of floe–eddy size ratios (figure 4). As discussed in the single floe analyses (§ 3.2), the observed variability arises from floe inertia, causing a delay in ice floe response to changes in the underlying ocean eddy field. This delay results in a discrepancy between the rotation of the ice floes and the underlying ocean eddies. Considering ice floe rotation rates normalised by the averaged ocean vorticity, ice floes behave as passive tracers provided $R_f/R_e \leqslant 0.7$ (figure 4*a*). However, as the floe–eddy size ratio increases and approaches 1.4, the peaks in the normalised rotation rates shift to greater values, reaching approximately 1.8, similar to the case of centred ice floes (figure 3*a*). Around $R_f/R_e \approx 0.5$, the distribution narrows and exhibits higher peaks, suggesting that a solid body rotation approximation accurately captures floe motion within this range of floe–eddy size ratios. This behaviour can be attributed to the ice floe area filtering out ice floe–ocean stress, thereby reducing ice floe responsiveness to any variability within the vortex cell. As floe–eddy size ratios increase, excessive filtering of ocean information over the ice floe diminishes sensitivity to underlying ocean characteristics, resulting in a broadening of the PDF. For ice floe rotation rates normalised by the ocean vorticity at the floe centre of mass, ice floes behave as passive tracers when $R_f/R_e \leqslant 0.25$. The peaks of the PDF shift to smaller values as the size ratios increase, reaching approximately 0.25 at $R_f/R_e = 1.4$ (figure 4*b*). Similar to the behaviour observed for averaged ocean vorticity, the distributions are more dispersed for small floes, while clear peaks are evident for $R_f/R_e \geqslant 0.25$, as the centre-of-mass ocean vorticity for larger floes tends to exceed the area-averaged vorticity.

Following the same approach as for centred ice floes, we derived analytical relations for the off-centred floes. By employing the Taylor series expansion, the analytical relations for the ice floe rotation rate normalised by the averaged ocean vorticity can be derived as

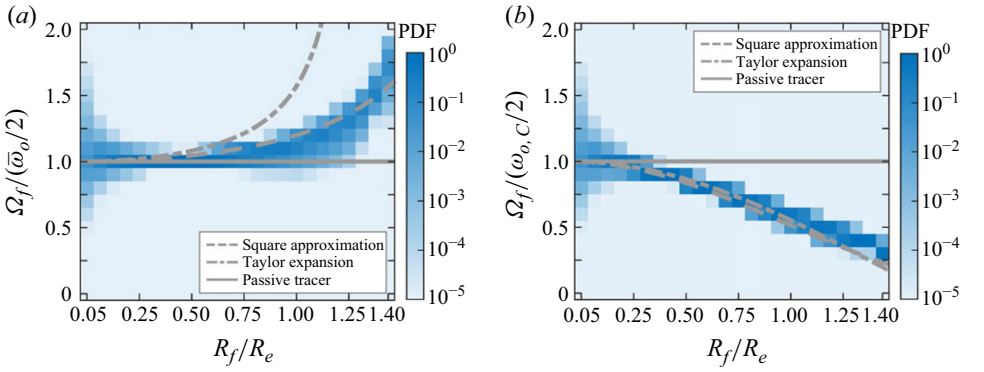

Figure 4. Rotational motion of off-centred ice floes in a TG vortex field. The PDFs of ice floe rotation rates, Ω_f, normalised by the (*a*) ocean vorticity averaged over the floe area, $\overline{\omega}_o$, and the (*b*) ocean vorticity at the floe centre of mass, $\omega_{o,C}$, for different floe–eddy size ratios. The simulation results are compared with analytical relations using square-shape approximation (dashed lines) and Taylor series expansion (dashed-dotted lines), and the passive tracer case (solid lines).

$$\frac{\Omega_f}{\overline{\omega}_o/2} = \frac{\left\{1 - \frac{\pi^2}{8}\left[\frac{\gamma^2}{3} + \left(\frac{r_f}{R_e}\right)^2\right] + \frac{\pi^4}{64}\left[\frac{\gamma^4}{48} + \frac{\gamma^2}{6}\left(\frac{r_f}{R_e}\right)^2 + \left(\frac{x_f}{R_e}\right)^2\left(\frac{y_f}{R_e}\right)^2\right]\right\}}{\left\{1 - \frac{\pi^2}{8}\left[\frac{\gamma^2}{2} + \left(\frac{r_f}{R_e}\right)^2\right] + \frac{\pi^4}{64}\left[\frac{\gamma^4}{24} + \frac{\gamma^2}{4}\left(\frac{r_f}{R_e}\right)^2 + \left(\frac{x_f}{R_e}\right)^2\left(\frac{y_f}{R_e}\right)^2\right]\right\}}, \tag{3.6}$$

where x_f and y_f are the horizontal Cartesian coordinates of the floe centre of mass, respectively, and $r_f = \sqrt{x_f^2 + y_f^2}$ is its radial position. Similarly, the ice floe rotation rate normalised by the centre-of-mass ocean vorticity can be then expressed as

$$\frac{\Omega_f}{\omega_{o,c}/2} = \frac{\left\{1 - \frac{\pi^2}{8}\left[\frac{\gamma^2}{3} + \left(\frac{r_f}{R_e}\right)^2\right] + \frac{\pi^4}{64}\left[\frac{\gamma^4}{48} + \frac{\gamma^2}{6}\left(\frac{r_f}{R_e}\right)^2 + \left(\frac{x_f}{R_e}\right)^2\left(\frac{y_f}{R_e}\right)^2\right]\right\}}{\left[1 - \frac{\pi^2}{8}\left(\frac{r_f}{R_e}\right)^2 + \frac{\pi^4}{64}\left(\frac{x_f}{R_e}\right)^2\left(\frac{y_f}{R_e}\right)^2\right]}. \tag{3.7}$$

In contrast to the centred ice floe cases, relations (3.6) and (3.7) not only depend on the floe–eddy size ratio, but also on the radial positions of the ice floes. Therefore, the normalised rotation rates were averaged over all r_f values for each of the floe–eddy size ratio bins. As $r_f \to 0$, the analytical relations for the off-centred floes (3.6) and (3.7) converge to the relations for the centred floes (3.2) and (3.3). Equation (3.6) is in good agreement with the PDF peaks for small floe–eddy size ratios (figure 4*a*). Their differences become evident around $R_f/R_e \approx 0.5$ and become more pronounced for larger size ratios due to the issues of the Taylor series expansion near the cell edges. Conversely, (3.7) closely aligns with the PDF peaks of ice floe rotation rates normalised by the centre-of-mass vorticity for most floe–eddy size ratios (figure 4*b*).

The square-shape approximation for off-centred floes yields the same analytical relations as for centred floes. Thus, (3.4) and (3.5) are also used to describe the rotation rates of off-centred floes. These equations match the PDF peaks over a wide range of floe–eddy size ratios and only show minor deviations at ratios around $R_f/R_e = 1.4$

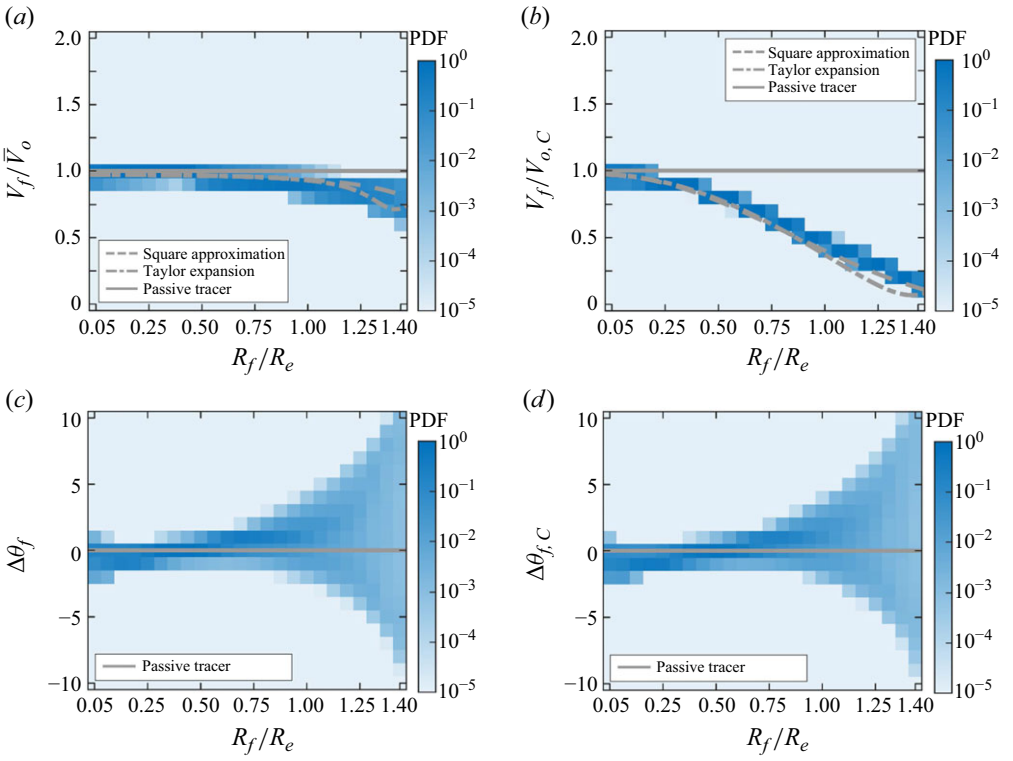

Figure 5. Translational motion of off-centred ice floes in a TG vortex field. The PDFs of ice floe speed, V_f, normalised by the (*a*) ocean speed averaged over the floe area, $\overline{V}_o$, and the (*b*) ocean speed at the floe centre of mass, $V_{o,C}$, and (*c* and *d*) angle deviations. For these last quantities, ice and ocean velocity angles are calculated using the direction of each velocity vector with respect to the positive x-axis, measured in the counter-clockwise direction. Then, deviations are computed by subtracting the angle of (*c*) the averaged ocean velocity, $\Delta\theta_f$, and the (*d*) centre-of-mass ocean velocity, $\Delta\theta_{f,C}$, from that of the ice floe velocity, for different floe–eddy size ratios. The simulation results are compared with analytical relations using square-shape approximation (dashed lines) and Taylor series expansion (dashed-dotted lines), and the passive tracer case (solid lines).

(figures 4*a* and 4*b*). Overall, the square-shape approximation provides accurate estimates of the PDF peak compared with the Taylor series approximation.

The PDFs of normalised ice floe speeds and floe–ocean angle deviations depend on the floe–eddy size ratios (figure 5), corresponding to the results of single floe analyses depicted in figure 2. For the ice floe speed normalised by the ocean speed averaged over the floe area, the PDF peaks at unity ($V_f/\overline{V}_o = 1$), resembling the behaviour of a passive tracer (figure 5*a*). As the floe–eddy size ratio increases and approaches 1.4, the normalised speed at the PDF peaks gradually decreases to $V_f/\overline{V}_o = 0.75$. In contrast to the ice floe rotation rate results, the PDFs of normalised floe speeds for small-sized floes exhibit narrow distributions. This trend can be attributed to the fact that the Coriolis force and the pressure gradient force due to the sea surface tilt depend on the velocity difference, $\Delta\mathbf{u}_f = \overline{\mathbf{u}}_o - \mathbf{u}_f$, while the torque generated by these forces depends solely on ocean velocity, $\overline{\mathbf{u}}_o$, with no contribution from the Coriolis force. As a result, floe speed is less responsive to changes in ocean speed. This is reflected in the third term of (2.9), which is derived using the geostrophic balance between the pressure gradient force due to sea surface tilt and the Coriolis force.

Overall, the ocean speed at the floe centre of mass is greater than the ocean speed averaged over the floe area. The peaks of the PDF for the floe speed normalised by the centre-of-mass ocean speed decrease to 0.25 as the floe–eddy size ratio increases to 1.4 (figure 5*b*). It is useful to note that the velocity difference between the ice floe and the underlying ocean remains relatively constant across different floe–eddy size ratios, such that $|\Delta \mathbf{u}_f| \approx C_0$, where C_0 denotes a constant. This value can be derived by equating the magnitude of the ice floe–ocean stress (the first term on the right-hand side of (2.9)) to a combination of the Coriolis force on the ice floe and the pressure gradient force due to the sea surface tilt (the third term on the right-hand side of (2.9)) under torque equilibrium, as follows: $|\Delta \mathbf{u}_f^*|^2/H_{f,o}^* \sim |\Delta \mathbf{u}_f^*|/Ro$. Then, the floe speed normalised by the averaged ocean velocity can be expressed as

$$\frac{V_f}{\overline{V}_o} \approx 1 - \frac{C_0}{\overline{V}_o}, \tag{3.8}$$

implying that, for lower averaged ocean speeds as in the case of larger floes, there is a reduction in normalised floe speeds.

Similar to (3.6)–(3.7), the analytical relation for ice floe speed normalised by the ocean speed averaged over the floe area and by the ocean speed at the floe centre of mass can be derived using the Taylor series expansion and the square-shape approximation. In relation (3.8), the averaged ocean speed can be approximated using a Taylor series expansion as follows:

$$\overline{V}_o = \left(\frac{\pi}{2}\right)^2 \left(\frac{A_{TG}}{R_e}\right) \left(\frac{r_f}{R_e}\right) M_o, \tag{3.9}$$

where $M_o = [(x_f/r_f)^2 M_{o,1}^2 + (y_f/r_f)^2 M_{o,2}^2]^{1/2}$. The parameters $M_{o,1}$ and $M_{o,2}$ are given by

$$\begin{aligned} M_{o,1} = 1 &- \frac{1}{12}\left(\frac{\pi}{2}\right)^2 \left\{3\gamma^2 + 2\left[\left(\frac{x_f}{R_e}\right)^2 + 3\left(\frac{y_f}{R_e}\right)^2\right]\right\} \\ &+ \frac{1}{96}\left(\frac{\pi}{2}\right)^4 \left\{\gamma^4 + 2\gamma^2\left[\left(\frac{x_f}{R_e}\right)^2 + 3\left(\frac{y_f}{R_e}\right)^2\right] + 8\left(\frac{x_f}{R_e}\right)^2\left(\frac{y_f}{R_e}\right)^2\right\}, \end{aligned} \tag{3.10a}$$

$$\begin{aligned} M_{o,2} = 1 &- \frac{1}{12}\left(\frac{\pi}{2}\right)^2 \left\{3\gamma^2 + 2\left[3\left(\frac{x_f}{R_e}\right)^2 + \left(\frac{y_f}{R_e}\right)^2\right]\right\} \\ &+ \frac{1}{96}\left(\frac{\pi}{2}\right)^4 \left\{\gamma^4 + 2\gamma^2\left[3\left(\frac{x_f}{R_e}\right)^2 + \left(\frac{y_f}{R_e}\right)^2\right] + 8\left(\frac{x_f}{R_e}\right)^2\left(\frac{y_f}{R_e}\right)^2\right\}. \end{aligned} \tag{3.10b}$$

Similarly, the ice floe speed normalised by the centre-of-mass ocean speed can be expressed using the averaged ocean speed as follows:

$$\frac{V_f}{V_{o,C}} = \left(1 - \frac{C_0}{\overline{V}_o}\right)\left(\frac{\overline{V}_o}{V_{o,C}}\right). \tag{3.11}$$

The centre-of-mass ocean speed can also be approximated using the Taylor series expansion

$$V_{o,C} = \left(\frac{\pi}{2}\right)^2 \left(\frac{A_{TG}}{R_e}\right) \left(\frac{r_f}{R_e}\right) M_{o,C}, \tag{3.12}$$

where $M_{o,C}$ is given by

$$M_{o,C}^2 = 1 - \frac{1}{3}\left(\frac{\pi}{2}\right)^2\left(\frac{r_f}{R_e}\right)^2\left[1+4\left(\frac{x_f}{r_f}\right)^2\left(\frac{y_f}{r_f}\right)^2\right]\left[1+\frac{1}{12}\left(\frac{\pi}{2}\right)^4\left(\frac{x_f}{R_e}\right)^2\left(\frac{y_f}{R_e}\right)^2\right] + \frac{1}{36}\left(\frac{\pi}{2}\right)^4\left(\frac{r_f}{R_e}\right)^4\left[1+18\left(\frac{x_f}{r_f}\right)^2\left(\frac{y_f}{r_f}\right)^2+\frac{1}{4}\left(\frac{\pi}{2}\right)^4\left(\frac{r_f}{R_e}\right)^4\left(\frac{x_f}{r_f}\right)^4\left(\frac{y_f}{r_f}\right)^4\right]. \tag{3.13}$$

Note that, for comparison with the simulation results, the normalised floe speeds in the analytical relations were averaged over all r_f values for each bin of floe–eddy size ratios. Similarly, using the square-shape approximation, the averaged ocean speeds can be approximated as the following:

$$\overline{V}_o = \left(\frac{\pi}{2}\right)\left(\frac{A_{TG}}{R_e}\right)\left[\sin\left(\frac{\pi\gamma}{2}\right)\Big/\left(\frac{\pi\gamma}{2}\right)\right]^2 \times\left[\cos^2\left(\frac{\pi}{2}\frac{x_f}{R_e}\right)\sin^2\left(\frac{\pi}{2}\frac{y_f}{R_e}\right)+\sin^2\left(\frac{\pi}{2}\frac{x_f}{R_e}\right)\cos^2\left(\frac{\pi}{2}\frac{y_f}{R_e}\right)\right]^{1/2}. \tag{3.14}$$

The centre-of-mass ocean speed can also be obtained as

$$V_{o,C} = \left(\frac{\pi}{2}\right)\left(\frac{A_{TG}}{R_e}\right)\left[\cos^2\left(\frac{\pi}{2}\frac{x_f}{R_e}\right)\sin^2\left(\frac{\pi}{2}\frac{y_f}{R_e}\right)+\sin^2\left(\frac{\pi}{2}\frac{x_f}{R_e}\right)\cos^2\left(\frac{\pi}{2}\frac{y_f}{R_e}\right)\right]^{1/2}. \tag{3.15}$$

The analytical relation using the square-shape approximation ((3.14) and (3.15)) shows good agreement with the peaks of the normalised speeds, while the analytical relation using the Taylor series expansion ((3.9) and (3.12)) exhibits deviations for $R_f/R_e \geqslant 1$ (figures 5*a* and 5*b*). The constant $C_0 = 0.15$ was chosen, producing the best-fit to the PDF peaks. Note that as $r_f \to 0$, the analytical relations for the normalised floe speed ((3.8) and (3.11)) converge to the centred floe case, as expected.

The PDFs of the angle deviation between ice floe velocity and ocean velocity are also contingent on the floe–eddy size ratio (figures 5*c* and 5*d*). As discussed in the single floe analysis (figure 2), the velocity of larger floes exhibits greater deviations from ocean velocity, including the averaged ocean velocity and the centre-of-mass velocity, thus resulting in more dispersed distributions for larger floe–eddy size ratios. While the vectors of the averaged ocean velocity and the centre-of-mass ocean velocity differ slightly in magnitude, their orientations are the same. This observation can be readily confirmed using the square-shape approximation, as follows:

$$\tan\overline{\theta}_o = -\tan\left(\frac{\pi}{2}\frac{x_f}{R_e}\right)\Big/\tan\left(\frac{\pi}{2}\frac{y_f}{R_e}\right) = \tan\theta_{o,C}, \tag{3.16}$$

indicating that the angle of the averaged ocean velocity is equal to the angle of the centre-of-mass ocean velocity.

In addition to calculating ocean velocity and vorticity beneath single ice floes, we can also compute local ocean vorticity from Green's theorem by using ice floe trajectory information. Passive tracers trapped in an eddy exhibit closed-loop trajectories. In this case, we can estimate the averaged ocean vorticity of the region enclosed by the trajectory as $\tilde{\omega}_o = \int \mathbf{u}_{tr}\cdot \mathrm{d}\mathbf{S}_{tr}$, where $\mathbf{u}_{tr}$ is the tracer velocity, $\mathbf{S}_{tr}$ is the tracer trajectory and $\sim$ denotes the averaged quantity over the closed region. Here, since $\mathbf{u}_{tr} = \mathbf{u}_o$, the true ocean vorticity, $\tilde{\omega}_o$, can be obtained. Similarly, trapped ice floes have been observed to form

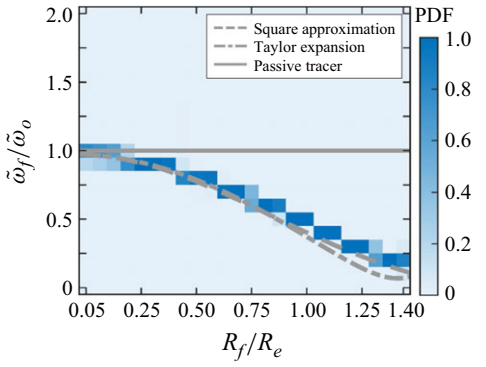

Figure 6. Averaged ocean vorticity estimates from ice floe trajectories in a TG vortex field. The PDFs of ratios between the averaged ocean vorticity of the region enclosed by ice floe trajectories, $\tilde{\omega}_f$, and true averaged ocean vorticity of the region, $\tilde{\omega}_o$, for different floe–eddy size ratios. The simulation results are compared with analytical relations using the square-shape approximation (dashed line) and Taylor series expansion (dashed-dotted line), and the passive tracer case (solid line).

nearly closed-loop patterns, with the endpoints slightly offset from the starting points. However, as previously discussed, the velocity of ice floes corresponds to the filtered ocean velocity over the floe area but is not exactly the same. As a result, any averaged ocean vorticity estimate within a trajectory-enclosed region, $\tilde{\omega}_f$, does not match the true averaged ocean vorticity of the same region, $\tilde{\omega}_f \neq \tilde{\omega}_o$. Nonetheless, their ratios can be approximated using the ice floe and underlying ocean velocities as

$$\frac{\tilde{\omega}_f}{\tilde{\omega}_o} = \frac{\oint \mathbf{u}_f \cdot \mathrm{d}\mathbf{S}_f}{\oint \mathbf{u}_{o,C} \cdot \mathrm{d}\mathbf{S}_f} \approx \frac{V_f}{V_{o,C}}, \tag{3.17}$$

where $\mathbf{u}_{o,C}$ is the ocean velocity at the floe centre of mass and $\mathbf{S}_f$ is the ice floe trajectory.

Floe trajectories are not perfectly closed, with just a short segment between the start and endpoints. Hence, the line integration in (3.17) is conducted from the first to the last points. The true averaged ocean vorticity can be calculated by integrating the centre-of-mass ocean velocity along the floe trajectory. The ratio of the ocean vorticity estimate based on ice floe velocity to the true ocean vorticity, $\tilde{\omega}_f/\tilde{\omega}_o$, can be approximated by the normalised ice floe speed, $V_f/V_{o,C}$ (3.17).

The PDFs of the ratio between the ocean vorticity estimate and the true ocean vorticity depend on floe–eddy size ratios (figure 6). The floe speed normalised by the centre-of-mass ocean speed significantly decreases for larger floe–eddy size ratios (figure 5*b*), resulting in smaller vorticity ratios. Furthermore, the peaks of the PDF for most floe–eddy size ratios align with the analytical relation for normalised floe speed using the square-shape approximation ((3.11), (3.14) and (3.15)). The relation using the Taylor series expansion ((3.11)–(3.13)) is in good agreement with the PDF peaks for $R_f/R_e \leqslant 0.75$, showing a discrepancy for larger ratios due to the coverage limit of the Taylor series expansion near the edge of the vortex cell.

3.3. *Statistics of ice floe kinematics in a QG flow field*

We performed simulations of ice floes in a QG flow field to apply the derived analytical relations to a more realistic ocean eddy field (figure 7). Passive tracers were released into the flow field, and ocean vorticity was interpolated to the Lagrangian tracer positions. Then, a LAVD-based eddy detection method (Haller *et al.* 2016) was used to identify the boundaries of eddies by searching for the outermost closed contour of the LAVD, which

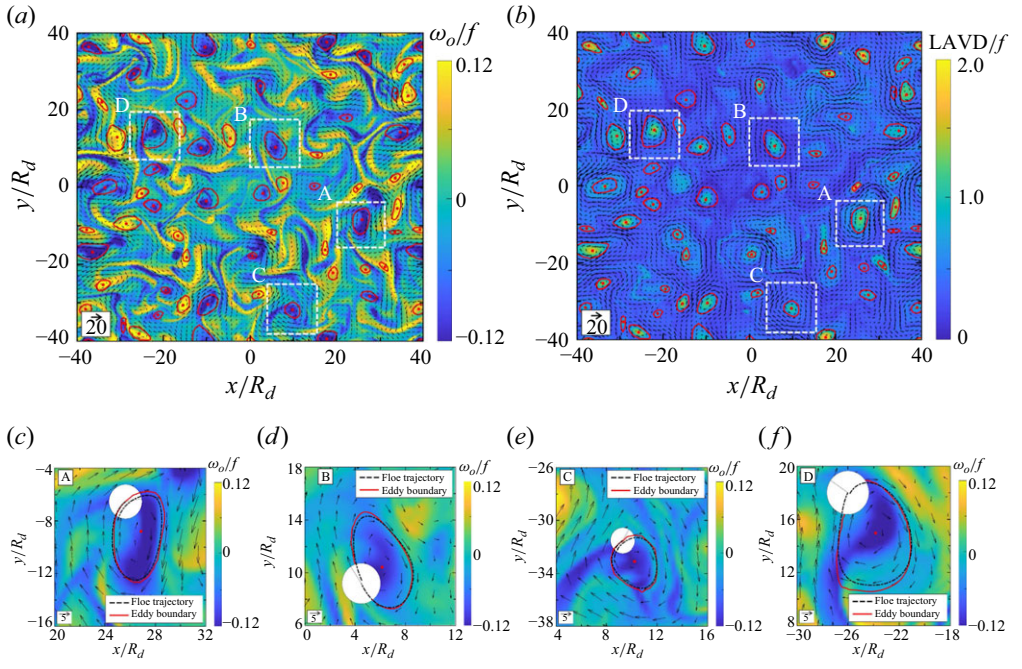

Figure 7. Motion of ice floes in a QG flow field. Boundaries (red lines) and centres (red dots) of the detected eddies are shown in the field of (*a*) ocean vorticity and (*b*) LAVD normalised by the Coriolis parameter f. (*c*–*f*) Representative cases of trajectories (black dashed lines) of trapped ice floes within local eddies marked as *A* to *D* with white dashed boxes in the QG and LAVD flow fields, respectively. The colour and arrows in the figure correspond to the magnitude of the normalised vorticity and LAVD and the magnitude and direction of the velocity at a given location, respectively. The floes (white circle) are positioned at the endpoint of their trajectories.

indicates local rotation relative to mean rotation. The LAVD was computed by averaging the vorticity deviation along the Lagrangian tracer trajectory as follows:

$$\mathrm{LAVD}\,(x_0,\,y_0) = \omega_o'\left[X\,(x_0,\,y_0)\,,\,Y\,(x_0,\,y_0)\right], \tag{3.18}$$

where $(X,\,Y)$ are the coordinates of tracers with an initial position of $(x_0,\,y_0)$, and ω_o' is the vorticity deviation from the spatial average over the whole domain. Given that the ocean field is time-independent in the present study, the time component is not considered in (3.18). A total of 70 eddies were identified in the QG flow field (figure 7*a*); their morphologies become more apparent in the LAVD field (figure 7*b*). Note that the LAVD has been widely used to capture vorticity-dominated structures in atmospheric and oceanic flows and has also been used as a baseline for evaluating trajectory-based diagnostics to quantify the kinematics of an underlying fluid (Aksamit *et al.* 2024). By leveraging the rotational relationship between floes and underlying eddies, the LAVD has the potential to be applied to the trajectories and rotation rates of ice floes for eddy detection purposes.

We selected four varying-size representative eddy cases to examine the kinematic link between drifting ice floes and the underlying flow field (figure 7*c*–*f*). To this end, we randomly released over 2,000 ice floes near each eddy, identifying floes trapped within vortex cores (Appendix A). Ice floes released near the eddy boundary exhibited nearly closed-loop trajectories resembling the shapes of the eddies (figure 7*c*–*f*). Hence, the trajectories of individual trapped ice floes provide a direct estimate of local eddy length scales, whereby the size of the largest enclosed region by ice floe trajectories,

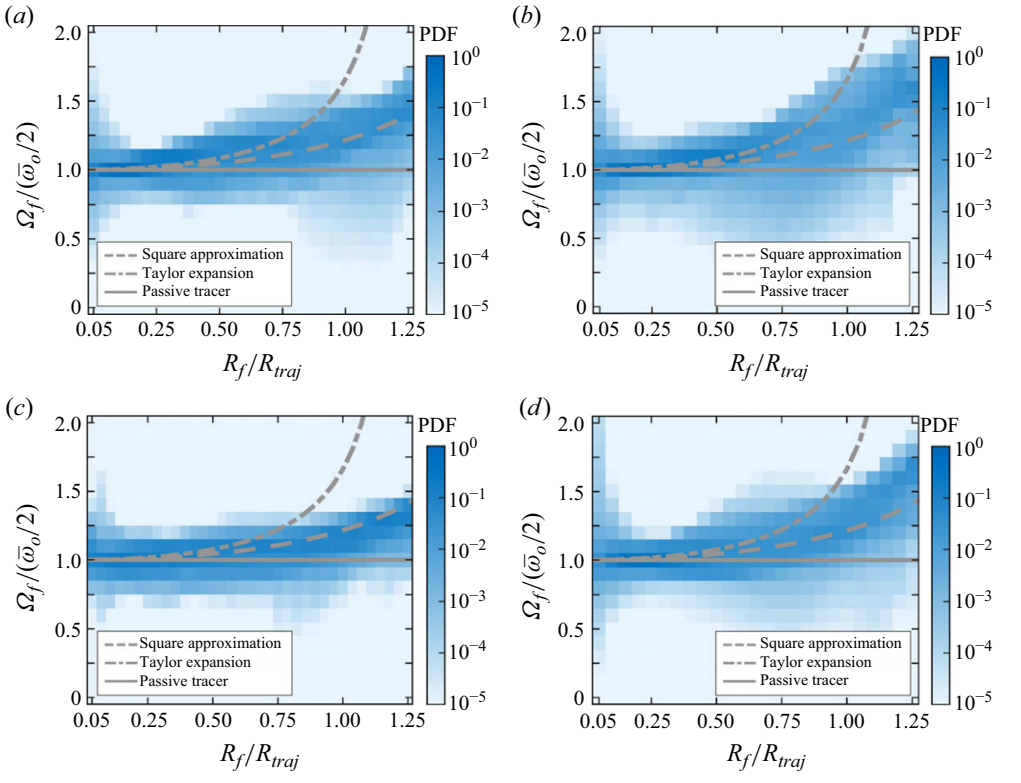

Figure 8. Rotational motion of trapped ice floes in local QG eddies. (*a–d*) The PDFs of ice floe rotation rates, Ω_f, normalised by the averaged ocean vorticity over the floe area, $\overline{\omega}_o$, for different ratios between floe size and trajectory-derived length scale, R_f/R_{traj}, in local eddies marked as A to D with white dashed boxes in a QG flow field, respectively. The simulation results are compared with analytical solutions using square-shape approximation (dashed line), Taylor series expansion (dashed-dotted line) and the passive tracer case (solid line).

$R_{traj} = \sqrt{A_{traj}/\pi}$, was chosen as a trajectory-derived length scale for each local eddy. Here, A_{traj} is the area of the largest enclosed region by ice floe trajectories. This length scale closely matches the eddy size in the TG vortex.

In QG eddies, ice floes simultaneously covering both the inside and outside regions of an eddy often become entrapped by the eddy, resulting in minor discrepancies between eddy size and trajectory-derived length scales. These differences arise due to variations in vorticity and velocity distributions among different QG eddies, leading to diverse trajectory shapes and trajectory-derived length scales. In the selected QG eddies, R_f/R_{traj} range from 0.05 to 1.25. Beyond these ranges, ice floes generally remain translating near the eddies or drift away from them over the simulation period.

We investigated the rotational relationship between trapped ice floes and the underlying local eddies for the four eddies marked in figure 7. Despite variations in eddy size and shape, the normalised rotation rates of ice floes showed similar qualitative and quantitative trends to those in the idealised vortex cases (figure 8). Notably, the PDFs of ice floe rotation rates, normalised by the ocean vorticity averaged over the floe area, peak at unity when $R_f/R_{traj} \leqslant 0.5$ for all four cases (figure 8). Note that the distributions of the normalised floe rotation rates in the QG eddy cases are more dispersed than in the TG vortex cases. We attribute this discrepancy to the highly nonlinear, deformed eddies dominant in the QG flow field. The PDF peaks become more pronounced in the QG cases as the floe size

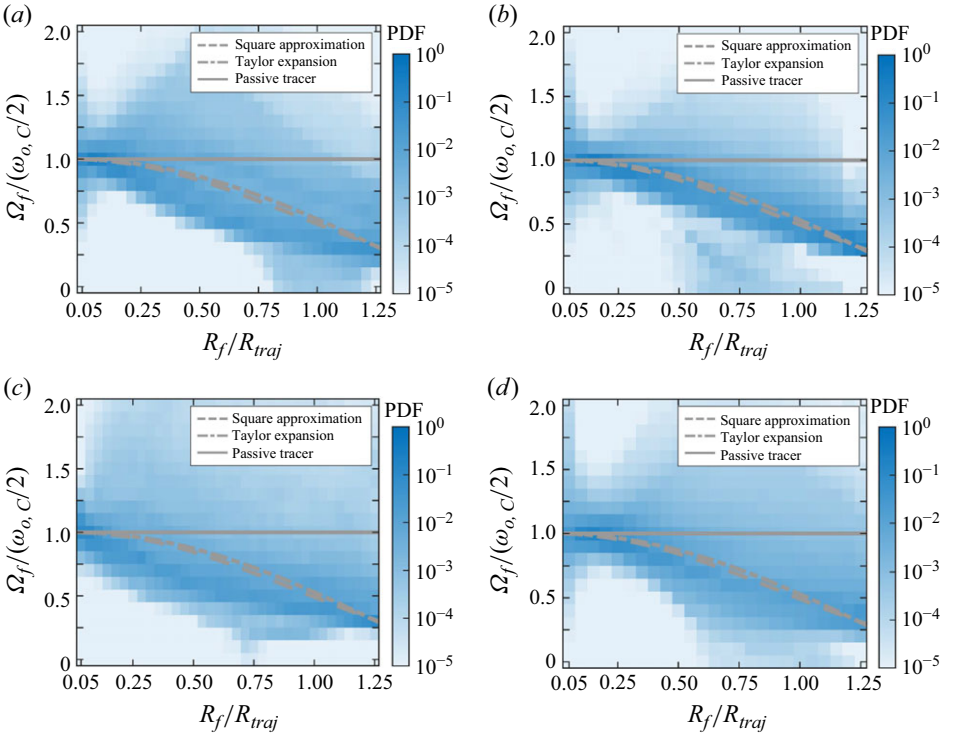

Figure 9. Rotational motion of trapped ice floes in local QG eddies. (*a–d*) The PDFs of ice floe rotation rates, Ω_f, normalised by the ocean vorticity at the floe centre of mass, $\omega_{o,C}$, for different ratios between floe size and trajectory-derived length scale in local eddies marked as *A* to *D* with white dashed boxes in a QG flow field, respectively. The simulation results are compared with analytical solutions using square-shape approximation (dashed line), Taylor series expansion (dashed-dotted line) and the passive tracer case (solid line).

approaches half of the trajectory-derived length scale ($R_f/R_{traj} = 0.5$). The peaks shift toward 1.5 as R_f/R_{traj} hits 1.25. Analytical relations derived for the TG vortex effectively characterise this behaviour. The relation from the Taylor series expansion (3.6) aligns with PDF peaks for smaller R_f/R_{traj}, while the relation from the square-shape approximation (3.4) agrees well with the peaks across most size ratios.

The PDFs of ice floe rotation rates normalised by the ocean vorticity at the floe centre of mass exhibit similar qualitative behaviours compared with the idealised vortex case (figure 9). As R_f/R_{traj} increases to 1.25, the PDF peaks decrease to 0.25, consistent with the TG vortex cases (figure 4*b*). However, analytical relations (3.5) and (3.7), derived for the TG vortex, exhibit discrepancies with the PDF peaks due to differences in the eddy structures of the flow fields. Vorticities near the centre of QG eddies exhibit smaller spatial gradients compared with the TG vortex, leading to smaller normalised rotation rates in the QG eddy cases. In addition, the centre-of-mass ocean vorticity changes abruptly across regions, contrasting with the averaged ocean vorticity, such that the rotation rates normalised by the centre-of-mass ocean vorticity show more discrepancies with the TG vortex cases and analytical relations derived for them.

The ocean vorticity estimate of the region enclosed by ice floe trajectories in QG eddies exhibits similar trends to the estimate in the TG vortex (figure 10). The PDFs of the ratio between the ocean vorticity estimate and true ocean vorticity reach their peaks at unity. However, these peaks decrease to 0.25 for larger R_f/R_{traj}, reaching up to 1.25. This trend is likely due to a greater discrepancy between the averaged ice floe velocity and the ocean

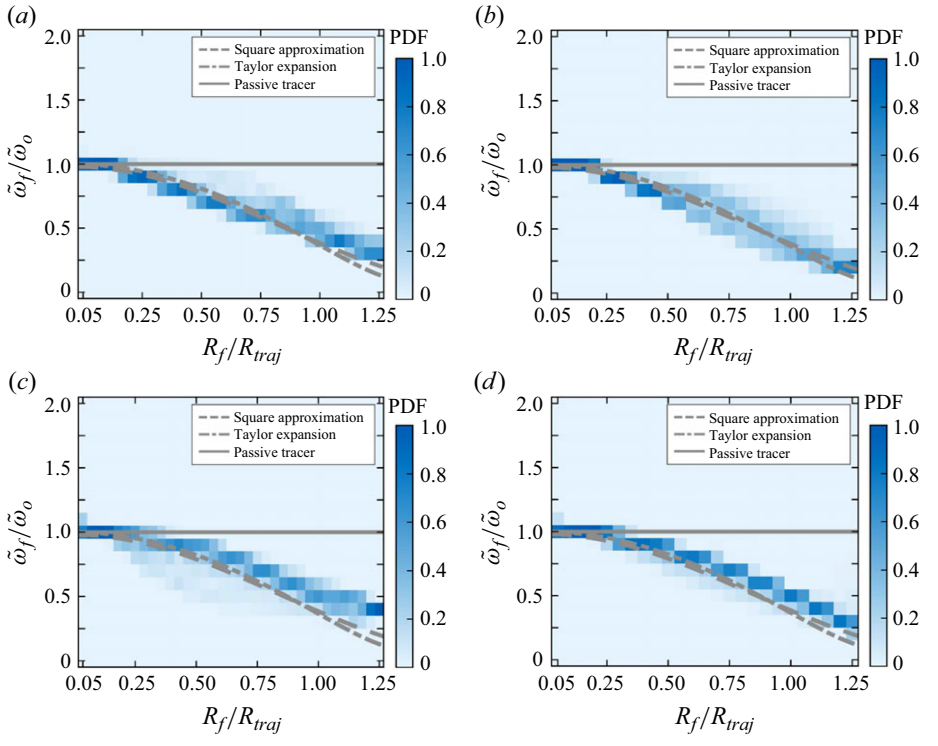

Figure 10. Averaged ocean vorticity estimate using ice floe trajectories in local QG eddies. (*a–d*) The PDFs of ratios between averaged ocean vorticity of the floe trajectory-enclosed region, $\tilde{\omega}_f$, and true averaged ocean vorticity of the same region, $\tilde{\omega}_o$, for different ratios between floe size and trajectory-derived length scale in local eddies marked as *A* to *D* with white dashed boxes in a QG flow field, respectively. The simulation results are compared with analytical solutions using square-shape approximation (dashed line), Taylor series expansion (dashed-dotted line) and the passive tracer case (solid line).

velocity at the floe centre of mass in QG eddies. Overall, analytical relation (3.17) captures the qualitative behaviour of the PDF peaks, albeit with minor quantitative discrepancies observed for certain R_f/R_{traj}.

The observed ice floe motions and their analytical relations to the ocean, derived from the idealised eddies, offer insights into the rotational relationship between ice floes and local eddies in the QG flow field. These findings demonstrate the potential applicability of these derived relations to analyse ocean eddies and estimate their vorticity using ice floes. The complexity in the QG case stems from how each eddy exhibits a unique structure, velocity and vorticity distribution, as illustrated in figure 7. These fundamental differences between the TG vortex and QG eddies limit the direct application of these relationships to QG fields. Nonetheless, further investigation, including analysing the effects of deformed eddy configurations and different vortex types, holds promise for developing a comprehensive framework to characterise the ocean eddy field from ice floe satellite remote sensing observations.

4. Discussion and further analyses

Following the analysis with idealised free-drifting ice floes, we investigated additional relevant factors influencing the link between ice floe rotation and the vorticity of underlying ocean eddies. Specifically, we discuss the effects of ice floe thickness,

atmospheric winds and floe–floe collisions, corresponding to specific sea ice concentrations, on the rotational relationship between ice floes and the TG vortex.

4.1. *Effects of ice floe thickness on ice floe kinematics*

The motion of ice floes is affected by their inertia, which is closely linked to their thickness. Thicker ice floes inherently possess greater inertia than thinner floes, leading to increased discrepancies between ice floe motions and the underlying ocean kinematics. Observations of ice floe thickness in the BG MIZ are limited (Haas & Druckenmiller 2009), but estimates typically fall within the order of $O(0.1)$ m during the spring-to-summer season (Manucharyan *et al.* 2022), especially for young and first-year ice, as estimated based on upward-looking sonars (Krishfield *et al.* 2014). To assess the influence of thickness on our results, we performed additional simulations considering floes with ice floe thicknesses ranging from 0.1 to 1 m, corresponding to $H^*_{f,o} = 1.0 \times 10^{-3}$–$1.0 \times 10^{-2}$, for three different floe–eddy size ratios. We examined the PDFs of normalised ice floe rotation rates and the trajectory-derived ocean vorticity estimates.

The sensitivity of the rotational relationship to ice floe thickness depends on the floe–eddy size ratio, with smaller ice floes being the most responsive to changes in ice floe thickness (figure 11). For $R_f/R_e = 0.1$, the PDFs of the normalised rotation rate consistently peak at unity (figures 11*a* and 11*b*). However, as ice floes become thicker, their inertia increases, leading to greater deviations in their rotation from the ocean rotation. As a result, the peaks gradually diminish, and the distributions become more dispersed. In addition, thicker ice floes tend to follow a more pronounced spiral trajectory, resulting in skewed distributions toward larger normalised rotation rates. Similarly, the PDFs of the ratio between averaged ocean vorticity estimates of the trajectory-enclosed region and true averaged ocean vorticity peak at unity (figure 11*c*). However, for thicker ice floes, the peaks gradually decrease, and the distributions become more dispersed and skewed toward lower ratios.

As the floe–eddy size ratio increases, the effect of ice floe thickness on the rotational relationship becomes relatively minor (figure 11*d–i*). Specifically, at $R_f/R_e = 0.5$, thicker ice floes exhibit more dispersed distributions for the rotation rate normalised by the averaged ocean vorticity, skewed toward larger values (figure 11*d*). In contrast, these floes show negligible changes in the rotation rate normalised by the centre-of-mass vorticity and in the averaged ocean vorticity estimates normalised by the true ocean vorticity (figures 11*e* and 11*f*). At $R_f/R_e = 1.0$, the PDFs become more dispersed compared with floes with $R_f/R_e = 0.5$ (figure 11*g–i*), as discussed in § 3. However, thicker ice floes exhibit nearly identical distributions to thinner ice floes, indicating negligible effects of ice floe thickness. Overall, thicker ice floes tend to follow more pronounced spiral trajectories due to their increased inertia. Nevertheless, these larger floes are less sensitive to changes in ocean information over the floe area, as this information is filtered out, resulting in minor changes in the rotational relationship between ice floes and the underlying ocean.

4.2. *Effects of atmospheric winds on ice floe kinematics*

While our analysis primarily focused on sea ice–ocean interactions, surface wind drag also influences ice floe motions in practical scenarios. Strong winds predominantly exert force on ice floes, potentially weakening the kinematic relationship to ocean vorticity and increasing uncertainty when inferring this information. Here, we investigate the effect of atmospheric winds on the rotational relationship between ice floes and the underlying ocean eddies by incorporating the surface wind drag term in (2.9) and (2.10) into our analysis.

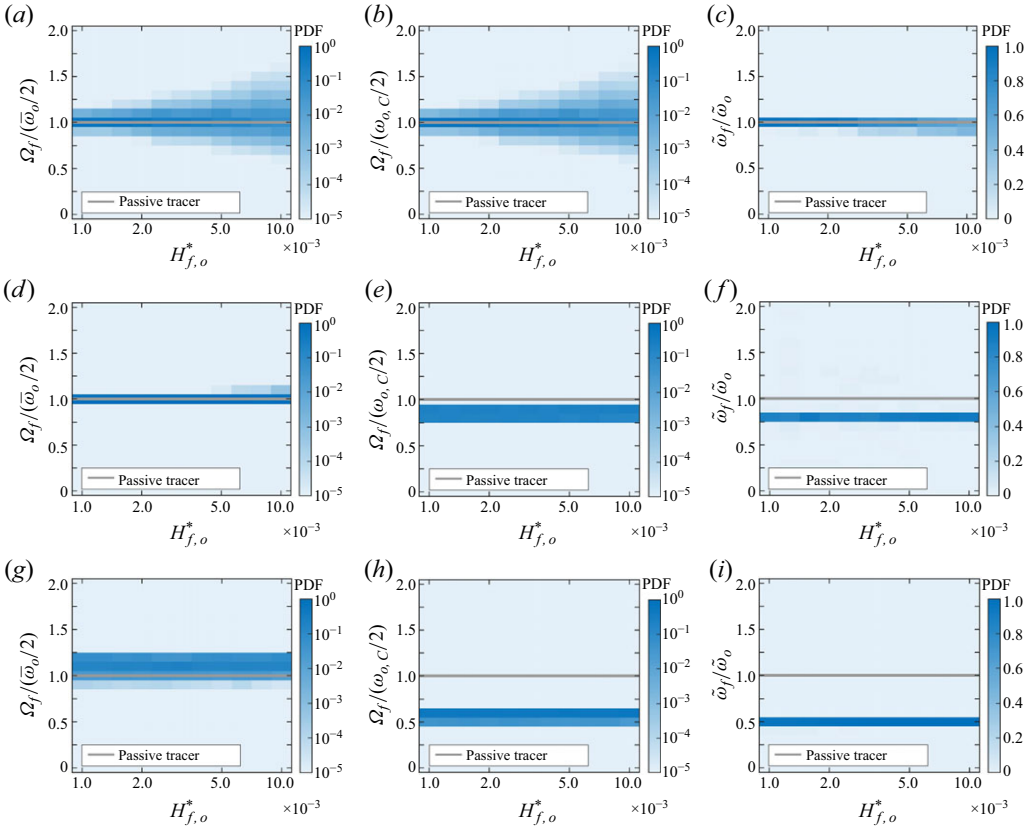

Figure 11. Motion of trapped ice floes with different thicknesses in a TG vortex. The PDFs of ice floe rotation rate, Ω_f, normalised by the (a, d, g) averaged ocean vorticity over the floe area, $\overline{\omega}_o$, and the (b, e, h) ocean vorticity at the floe centre of mass, $\omega_{o,C}$. and of (g, h, i) ratio between estimated ocean vorticity averaged over the trajectory-enclosed region, $\tilde{\omega}_f$, and true ocean vorticity of the same region, $\tilde{\omega}_o$, for different floe–eddy size ratios, $R_f/R_e = (a, b, c)$ 0.1, (d, e, f) 0.5 and (g, h, i) 1.0.

In general, atmospheric winds have larger length scales compared with upper-ocean eddies, potentially causing ice floes to trace straight trajectories rather than curved ones (Lopez-Acosta 2021; Manucharyan *et al.* 2022). Thus, we considered unidirectional atmospheric winds with consistent positive speeds across the entire domain in both the zonal and meridional directions. These winds do not directly affect the rotation of ice floes under homogeneous conditions (i.e. uniform surface roughness and thickness within floes). However, unidirectional winds influence the translational motion of the ice floes, leading to increased discrepancies between their rotations and the rotations of the underlying ocean.

We investigated the motion of ice floes under weak and strong wind conditions. In low winds, ice floes tend to remain within the vortex cell. In these cases, surface wind stress to surface ocean stress ratios, $\tau_{a,ref}/\tau_{o,ref}$, range from 0 to 0.1, and wind velocities have magnitudes from 0 to 2.5 m s^{-1}. Here, the stress ratio is calculated relative to zero ice floe speed. As wind speeds increase, the influence of wind forcing on ice floe motion becomes more significant, leading to ice floes escaping the vortex cell and a notable decrease in the number of trapped ice floes, especially the large floes. In high winds, stress ratios range from 0.2 to 2.0, and wind speeds vary from 2.5 to 10.6 m s^{-1}, corresponding to observed wind speeds in the MIZ (Kozlov & Atadzhanova 2022).

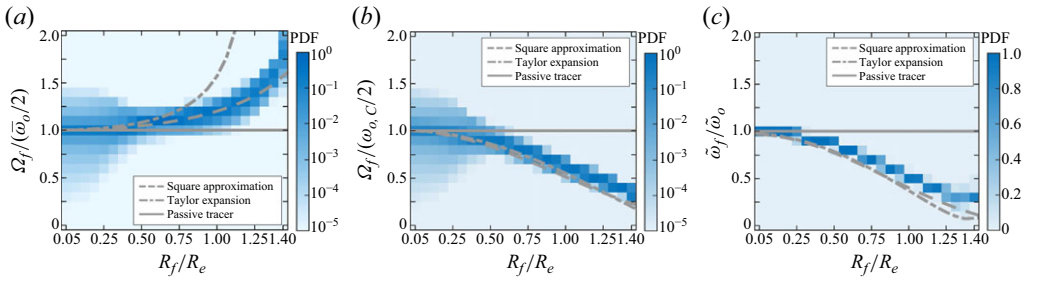

Figure 12. Motion of trapped ice floes in a TG vortex with low winds. The PDFs of ice floe rotation rate, Ω_f, normalised by the (*a*) averaged ocean vorticity over the floe area, $\overline{\omega}_o$, and the (*b*) ocean vorticity at the floe centre of mass, $\omega_{o,C}$, and (*c*) of the ratio between averaged ocean vorticity estimate of the trajectory-enclosed region, $\tilde{\omega}_f$, and true averaged ocean vorticity of the same region, $\tilde{\omega}_o$, for different floe–eddy size ratios. The wind stress to ocean stress ratio is $\tau_{a,ref}/\tau_{o,ref} = 0.1$. The simulation results are compared with analytical solutions using square-shape approximation (dashed line) and Taylor series expansion (dashed-dotted line), and the passive tracer case (solid line).

In low wind scenarios ($\tau_{a,ref}/\tau_{o,ref} = 0.1$), the PDFs of the normalised rotation rates and the ratios between averaged ocean vorticity estimates and true ocean vorticities exhibit similar peaks and distributions (figure 12) compared with those under zero wind conditions (figures 4 and 6). For normalised rotation rates, distributions become more dispersed for most floe–eddy size ratios, with peaks slightly shifting toward higher values due to wind forcing deforming ice floe trajectories toward cell boundaries. In addition, the analytical relations (3.4)–(3.7) and (3.17) align well with PDF peaks, demonstrating the potential applicability of these derived relations under low wind conditions.

In high winds, the effects of surface wind drag on the rotational relationship vary depending on the floe–eddy size ratios (figure 13). Note that all ice floes are considered in the analyses. For $R_f/R_e = 0.1$, the effects of wind forcing on the rotation rate normalised by the averaged ocean vorticity are negligible (figure 13*a*). However, wind forcing marginally decreases the peaks of the PDFs and results in slightly more dispersed distributions (figure 13*b*). As the floe–eddy size ratios increases, the effects of wind forcing become more pronounced, resulting in skewed distributions. For $R_f/R_e = 0.5$ and 1.0, the PDF peaks of rotation rates normalised by the averaged ocean vorticity shift toward greater values (figures 13*c* and 13*e*), whereas the peaks of rotation rates normalised by the centre-of-mass ocean vorticity shift toward lower values (figures 13*d* and 13*f*). The peak values in both cases decrease, and the distributions become more dispersed as the stress ratio increases from 0.1 to 0.5. Beyond this range, the PDFs begin to converge, showing minor differences in the distribution. The peaks slightly decrease, and the distributions become more dispersed at larger stress ratios.

Overall, the wind breaks off the influence of ocean eddies on ice floe rotation, with the effect being most pronounced under strong wind conditions. In such cases, ice floes tend to move around and along the boundaries of the vortex cell, where ocean and wind stresses are comparable, resulting in skewed distributions of normalised rotation rates. At the same stress ratios, larger floes show significant changes in the peaks and distributions of their rotation rates due to their greater coverage of the flow field.

4.3. *Effects of floe–floe collisions on ice floe kinematics*

Ice floes with no collisions are typically found in regions with low sea ice concentrations. In contrast, in areas of higher sea ice concentrations, floe–floe collisions become more common due to the densely packed distribution of ice floes (Leppäranta 2011) affecting

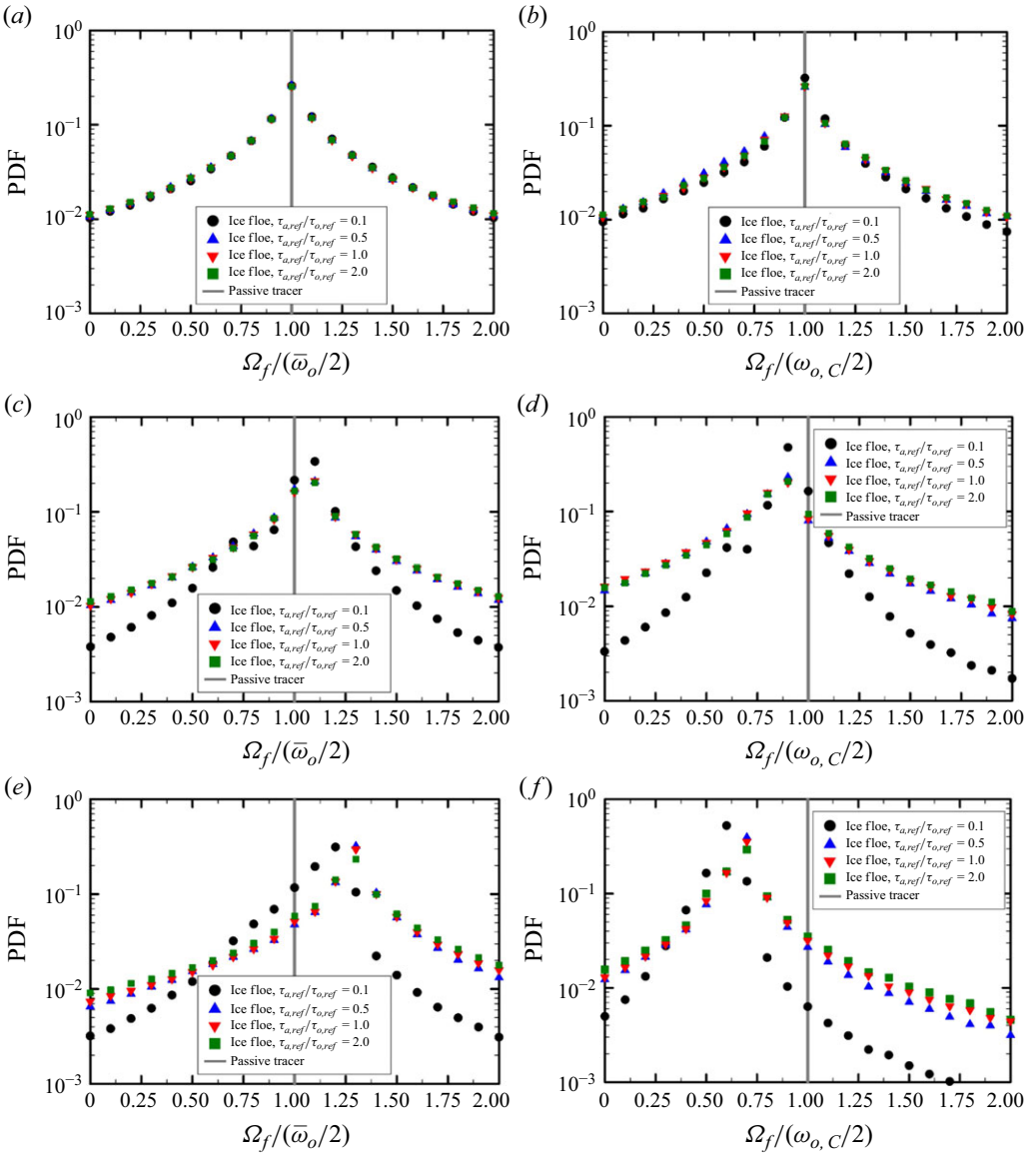

Figure 13. Motion of trapped ice floes in a TG vortex with high winds. The PDFs of ice floe rotation rate, Ω_f, normalised by the (a, c, e) averaged ocean vorticity over the floe area, $\overline{\omega}_o$, and the (b, d, f) ocean vorticity at the floe centre of mass, $\omega_{o,C}$, for different wind stress to ocean stress ratios, $\tau_{a,ref}/\tau_{o,ref} = 0.1$ (black circle), 0.5 (blue up-pointing triangle), 1.0 (red down-pointing triangle), and 2.0 (green square). The floe–eddy size ratios are $R_f/R_e = (a, b)$ 0.1, (c, d) 0.5, (e, f) 1.0. The simulation results are compared with the passive tracer case (solid line).

floe rotations (Brenner *et al.* 2023). These collisions exert contact forces that weaken the connection between ice floes and the underlying ocean, introducing noise into the estimation of ocean information through ice floe motions. In this section, we explored the effects of floe–floe collisions on the rotational relationship between ice floes and the underlying ocean to assess the feasibility of using ice floes with collisions for inferring ocean kinematics.

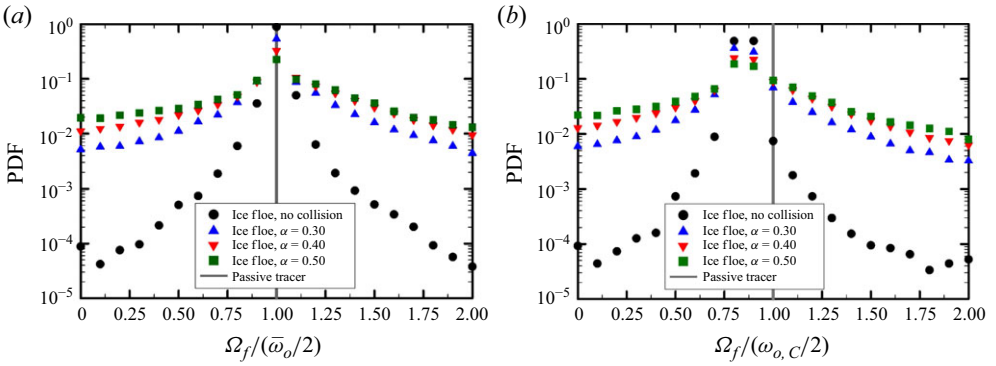

Figure 14. Motion of ice floes with collisions in a TG vortex. The PDFs of ice floe rotation rate, Ω_f, normalised by the (*a*) averaged ocean vorticity over the floe area, $\overline{\omega}_o$, and the (*b*) ocean vorticity at the floe centre of mass, $\omega_{o,C}$, for different sea ice concentrations, $\alpha = 0.30$ (blue up-pointing triangle), 0.40 (red down-pointing triangle) and 0.50 (green square). The floe–eddy size ratio is $R_f/R_e = 0.5$. The results are compared with the freely drifting floes (black circles) and the passive tracer case (solid lines).

Simulations were conducted with 2,000 randomly released ice floes, and rotation rate measurements began once the overlapping areas between ice floes were reduced to less than 10 % of their total area. Sea ice concentration was calculated as the total ice floe area divided by the size of the smallest rectangular domain confining all ice floes over the simulation time. Since the domain size is determined by the instantaneous positions of the ice floes, sea ice concentration can vary slightly over time. Thus, the time-averaged sea ice concentration was used to represent each simulation. In (2.7) and (2.8), the contact forces, $\mathbf{F}_{j,k}$, and the corresponding torques, $\mathbf{r}'_{j,k} \times \mathbf{F}_{j,k}$, were incorporated into the simulations. The simulation parameters are consistent with those described for ice floes in the BG MIZ, as detailed in Manucharyan *et al.* (2022) and summarised in table 1. For the ice floe set-up, the total of 2,000 ice floes was divided into smaller subsets to ensure that the number of collisions remained within specified ranges of interest while maintaining the desired sea ice concentration. Similar to the strong wind cases (§ 4.2), the simulated ice floes exhibited significant deviations from the closed-loop patterns observed in the idealised cases due to collisions and thus all results were indiscriminately considered.

We examined the PDFs of normalised ice floe rotation rates for different sea ice concentrations, α, and compared them with floes with no collisions (figure 14). As a representative case, we selected floes with $R_f/R_e = 0.5$, showing a clear peak in the PDFs. Sea ice concentrations ranging from $\alpha = 0.3$ to 0.5 were considered, reflecting typical moderate values in the MIZ, where concentrations range from $\alpha = 0.15$ to 0.80. Overall, the PDF peaks occur at the same rotation rates for different concentrations, but higher concentrations lead to more dispersed distributions. For rotation rates normalised by the averaged ocean vorticity, the PDF peak decreases from 0.89 (no collision case) to 0.22 ($\alpha = 0.5$) (figure 14*a*). Similarly, for rotation rates normalised by the centre-of-mass vorticity, the PDF peak decreases from 0.49 (no collision case) to 0.19 ($\alpha = 0.5$) (figure 14*b*). These changes are caused by increasing collision counts at higher concentrations, which reduce the influence of ocean vorticity on ice floe rotation. The average collision count increases from zero (no-collision case) to 160 ($\alpha = 0.5$). Despite these changes, the distributions retain their shapes across different concentrations, as collisions show no directional bias in altering floe rotation.

While sea ice concentration represents the overall fraction of ice floes in the domain, collision count reflects the extent of contact forces and corresponding torques affecting ice

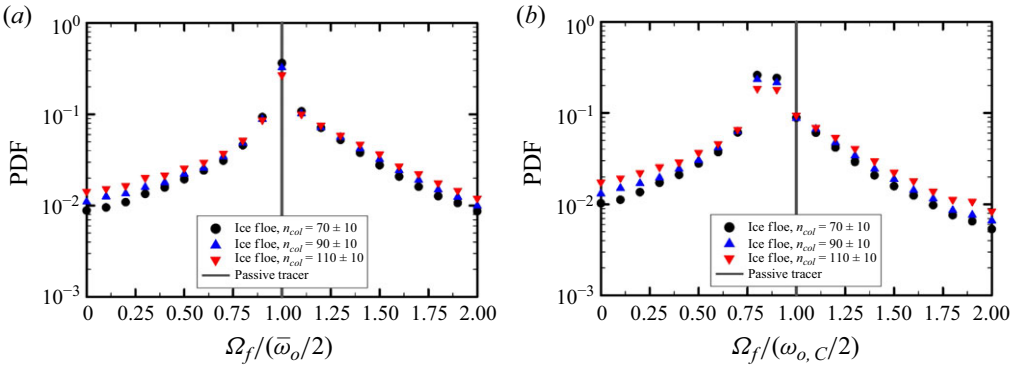

Figure 15. Motion of ice floes with collisions in a TG vortex. The PDFs of ice floe rotation rate, Ω_f, normalised by the (a) averaged ocean vorticity over the floe area, $\bar{\omega}_o$, and the (b) ocean vorticity at the floe centre of mass, $\omega_{o,C}$ for different collision count ranges, $n_{col} = 70 \pm 10$ (black circle), 90 ± 10 (blue up-pointing triangle) and 110 ± 10 (red down-pointing triangle). The floe–eddy size ratio is $R_f/R_e = 0.5$. The results are compared with the passive tracer case (solid lines).

floe motions. We compared the PDFs of normalised rotation rates for cases with different collision counts, $n_{col} = 70 \pm 10$, 90 ± 10, 110 ± 10, at $R_f/R_e = 0.5$ to assess the influence of floe–floe collisions (figure 15). Within each simulation run, the collision counts vary over time and only the time ranges corresponding to the selected collision counts were considered for the analysis. The PDFs consistently peak at the same rotation rates for different collision counts but become increasingly dispersed as collision counts rise. This behaviour aligns with the trends observed for different sea ice concentrations, in which higher concentrations generally coincide with more frequent collisions, assuming constant floe sizes.

Lastly, we explored the impacts of floe–eddy size ratios for the same collision count ranges. While sea ice concentration can be maintained through various combinations of floe sizes and the number of floes, it represents only the combined effects of these factors and is insufficient as a standalone control parameter. Instead, we used collision count as a control parameter to assess the influence of floe–eddy size ratios on ice floe rotation rates. The PDFs of normalised rotation rates for different floe–eddy size ratios were compared in the collision count range $n_{col} = 70 \pm 10$ (figure 16). Overall, the distributions exhibit qualitatively similar trends to the free-drifting cases (figure 4). The PDFs of floe rotation rates normalised by the averaged ocean vorticity exhibit distinct peak values and distributions for different floe–eddy size ratios (figure 16a). At $R_f/R_e = 0.1$, the PDF peaks at unity but has a more dispersed distribution compared with $R_f/R_e = 0.5$, where the PDF also peaks at unity. As R_f/R_e increases to 1.0, the PDF peak shifts to 1.1. The PDFs of floe rotation rates normalised by the centre-of-mass ocean vorticity peak at lower rotation rates and show greater skewness for larger R_f/R_e (figure 16b).

5. Conclusion

We quantified the kinematic relationship between ocean eddies with surface expression and floes trapped within their cores and derived analytical relations linking their rotations and velocities, with floe–eddy size ratios as a key parameter in the analysis. Our results show that ice floes can act as vorticity meters of the ocean even though the combined effects of floe inertia and the filtering effect of ocean information over the floe area produce differences between direct measurements of ocean velocities and rotations and

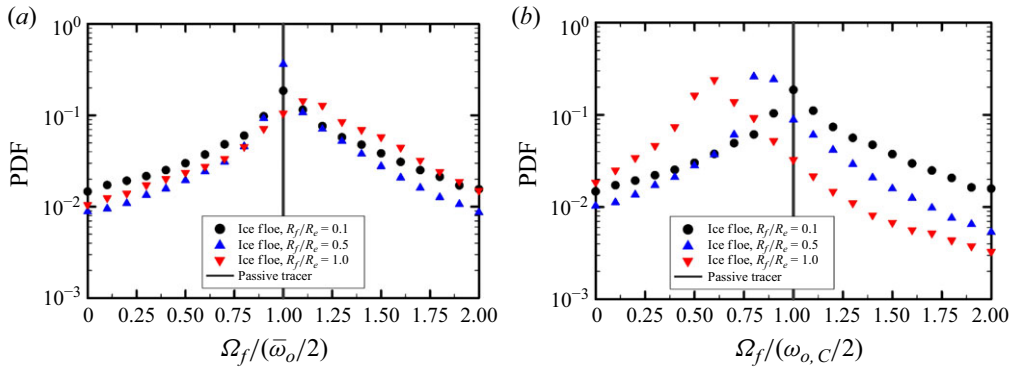

Figure 16. Motion of ice floes with collisions in a TG vortex. The PDFs of ice floe rotation rate, Ω_f, normalised by the (*a*) averaged ocean vorticity over the floe area, $\overline{\omega}_o$, and the (*b*) ocean vorticity at the floe centre of mass, $\omega_{o,C}$ for different floe–eddy size ratios, $R_f/R_e = 0.1$ (black circle), 0.5 (blue up-pointing triangle) and 1.0 (red down-pointing triangle). The collision count range is $n_{col} = 70 \pm 10$. The results are compared with the passive tracer case (solid lines).

estimates derived from ice floe observations. These findings and the derived analytical relations demonstrate the direct applicability of our methodology for inferring ocean eddy characteristics from ice floe remote sensing measurements.

We began our analysis with a TG vortex, employing two distinct vorticity metrics: averaged ocean vorticity over the floe area and ocean vorticity at the floe centre of mass. Our analysis revealed that in idealized vortices ice floes typically follow closed-loop trajectories, driven by the interplay of sea ice–ocean drag and a resultant force comprising the pressure gradient force due to sea surface tilt and the Coriolis force. Along these trajectories, the rotation rates and velocities of ice floes show oscillatory behaviour, undergoing alternating periods of acceleration and deceleration relative to the equilibrium values of force and torque. The floe rotation rate normalised by the area-averaged ocean vorticity underneath it increases with increasing floe–eddy size ratio for both centred and off-centred ice floes. This trend arises from the gradual decrease in local ocean vorticity from the centre of the TG vortex toward its boundaries. Ice floes behave as passive tracers when floe size is smaller than about 70 % of the eddy scale; however, as the floe–eddy size ratio increases to 1.4, the PDF peaks of rotation rates normalised by the averaged ocean vorticity shift toward higher values, reaching approximately 1.8. When floe size is about half the eddy scale, the distribution narrows and exhibits higher peaks, indicating that a solid body rotation approximation effectively describes ice floe motion within this range. Conversely, the rotation rate normalised by the centre-of-mass ocean vorticity decreases for large floe–eddy size ratios. The velocities of ice floes were also used to estimate the averaged ocean vorticity within regions enclosed by their trajectories. These estimates were smaller than the true ocean vorticity of the same region; their ratios can be described by the relationship between ice floe and ocean velocities.

To further understand this dynamics, we derived analytical relations for ice floe rotation rates and velocities using the Taylor series expansion and the square-shape approximation. While the Taylor series expansion agrees well with the PDF peaks for small floe–eddy size ratios ($R_f/R_e \leqslant 0.5$), the square-shape approximation aligns closely with the PDF peaks across a broader range of size ratios. Analytical relations for the ratio between the averaged ocean vorticity estimate and true ocean vorticity also show good agreement with the PDF peaks. These relations were applied to a more realistic ocean eddy field obtained from a two-layer QG model. The trends observed in the TG vortex are also

evident in the QG flow field when floe size is normalised by the trajectory-derived length scale. As the normalised floe size increases, the rotation rates normalised by the averaged ocean vorticity increase, while those normalised by the centre-of-mass ocean vorticity decrease. The derived relations closely match the PDF peaks for normalised rotation rates, demonstrating their potential applicability in inferring ocean kinematics through ice floe motions.

We closed our study by exploring other factors influencing the rotational relationship between ice floes and the underlying ocean, such as ice floe thickness, atmospheric winds and floe–floe collisions. For ice floe thicknesses ranging from 0.1 to 1 m, we found that thicker floes exhibit reduced PDF peaks and more dispersed distributions due to increased floe inertia. Interestingly, the impact of varying floe thickness lessens with increasing floe–eddy size ratios and becomes negligible at $R_f/R_e = 0.5$. We also examined atmospheric wind forcing under low and high wind conditions. Under low wind conditions, wind–sea ice stresses have a minor effect on the normalised rotation rates, causing their PDF peaks to shift slightly to higher values. In high wind conditions, the PDFs of normalised rotation rates are skewed as stress ratios increase. The PDFs converge under larger stress ratios for increasing floe–eddy size ratios (R_f/R_e =0.1–1.0). Finally, we investigated the impact of floe–floe collisions, which weaken the rotational link between ice floes and the underlying ocean. For $R_f/R_e = 0.5$, higher sea ice concentrations and larger collision counts lead to reduced PDF peaks and more dispersed distributions. When considering a fixed collision count ($n_{col} = 70 \pm 10$), the PDFs for different floe–eddy size ratios exhibit trends consistent with those observed in free-drifting cases.

5.1. *Directions for future research*

Our idealised simulations effectively capture the key rotational relationship between ice floes and the underlying ocean eddies in low-wind conditions and without significant floe interactions. However, incorporating additional ocean and ice floe observations may enhance the estimation accuracy of our framework for practical applications in ocean characterisation from ice floe remote sensing measurements.

The derived relations in the present study are applicable to both mesoscale and submesoscale motions in the ocean surface layer. These relations are particularly well suited for analysing eddies in the mesoscale regime ($Ro \ll 1$), where flows are predominantly horizontal and close to geostrophic balance (Taylor & Thompson 2023), resulting in rotation-dominant behaviours. In the submesoscale regime ($Ro \sim 1$), vertical motions and ageostrophic effects, such as convergence and divergence of flows, may introduce additional uncertainties into estimating ocean vorticity based on ice floe rotation rates. However, submesoscale motions still exhibit surface expressions at length scales comparable to the Rossby radius (5–15 km), similar to the smaller end of observed ice floe sizes (4–70 km) in Lagrangian ice floe datasets (Lopez-Acosta *et al.* 2019; Manucharyan *et al.* 2022), for which our framework is designed. At these scales, rotational flows remain more dominant than converging or diverging flows, preserving their two-dimensional characteristics. Nonetheless, a comprehensive assessment of the applicability of the derived relations to submesoscale motions is needed to improve accuracy in this regime.

In the Arctic ocean, inertial oscillations and internal tidal motions, occurring roughly twice a day (Gimbert *et al.* 2012; Watkins *et al.* 2023; Yuan *et al.* 2023), may influence the motion of small-scale ice floes on sub-daily time scales. However, their effects on floe rotation at the length and time scales applicable to satellite observations are likely to be negligible. Our framework is designed for datasets with daily resolution, capturing floes

with a size down to approximately 5 km. At these temporal and spatial scales, inertial and tidal oscillation effects would result from averaging oscillations over a few cycles with random phases for each floe observation and hence be expected to manifest as noise. Moreover, these oscillations primarily affect the trajectories of ice floes rather than their rotation rates about the centre of mass, with minimal impact on the rotational relationship between ice floes and the underlying ocean. As part of future work, the effects of inertial and internal tidal oscillations will be further investigated using high-resolution ocean–sea ice models or *in situ* buoy measurements, which provide higher temporal and spatial resolutions.

In addition to ocean characteristics, ice floes indeed show variability in their physical properties, such as non-circular shapes (e.g. polygons) and rheology. During late spring to summer, large ice packs crack and fracture along preferential directions, generating diverse floe sizes and shapes, which in turn influence ice floe rotation rates. Ice floes with anisotropic shapes would exhibit distinct rotational behaviours, which can be expected from the motion of small, micro-scale particles in turbulent flows (Parsa *et al.* 2012; Voth & Soldati 2017). These particles undergo rapid orientation changes due to intermittently large velocity gradients and tend to align with these gradients in the flow. A similar preferential alignment is expected for ice floes, which may orient along large velocity gradients in the flow, thereby influencing their rotation rates. Further investigation is needed to fully understand this effect.

The rheological properties of ice floes can influence their rotational motion. Collisions between ice floes, as well as the convergence and divergence of underlying oceanic flows, can induce internal stress within floes, leading to deformation (Gimbert *et al.* 2012; Yuan *et al.* 2023). This deformation can create inhomogeneities in ice floe thickness and surface topography (Feltham 2008), complicating the rotational relationship between ice floes and the ocean. Such effects may broaden the PDFs of the rotational relationship in our framework, increasing uncertainties in estimating ocean vorticity from ice floe rotation rates. However, in regions with low sea ice concentrations, where floe–floe collision rates are relatively low, treating ice floes as solid objects effectively captures the key features of the relationship. In addition, even in areas with high sea ice concentrations, our framework remains applicable to free-drifting ice floes – experiencing nearly zero internal stresses due to their consistent and unidirectional motion – for characterising large-scale ocean currents, as well as local eddies.

While the present study focuses on the dynamical behaviour of sea ice driven by ice–ocean drag, the thermodynamics of sea ice can influence the ice–ocean boundary layer, primarily through melting. Melting ice floes typically lower the surface temperature beneath them. During summer, substantial melting deposits freshwater to the ocean surface layer, creating sharp surface buoyancy gradients that drive mixed-layer instabilities (Shrestha & Manucharyan 2022; Gupta & Thompson 2022). These instabilities, in turn, generate submesoscale eddies and filaments near floe boundaries, which propagate from the ice edge toward floe centres. Such eddies can also transport ice floes into the open ocean, enhancing melting. In addition, induced vertical heat transport due to submesoscale motions may further increase ice floe melt rates (Horvat, Tziperman & Campin 2016; Gupta & Thompson 2022; Manucharyan & Thompson 2022). However, the effects of sea ice melting on the ice–ocean boundary layer become significant about a month after the onset of melting and have a reduced influence at low sea ice concentrations (Gupta & Thompson 2022); the conditions under which our framework is designed to operate. Furthermore, our framework focuses on ice floes during the spring-to-summer transition, whereas melting is generally more pronounced later in the summer.

Our findings and analytical relations provide a new framework for estimating local ocean vorticity with associated uncertainties. By incorporating Lagrangian observations of ice floe trajectories, rotation rates, velocities and shapes, the analytical relations can provide locally averaged ocean vorticities and velocities. Furthermore, PDFs of ice floe rotation rates enable the assessment of uncertainties in estimated ocean information. Beyond kinematic analyses, ice floe rotation rates, which contain local, spatial ocean information, have the potential to provide insights into ocean kinetic energy and enstrophy spectra, thereby aiding in the characterisation of energy cascades in mesoscale and submesoscale ranges. While the derived relations effectively describe the ice floe–ocean relationship, practical applications require further consideration of factors, including ocean characteristics (e.g. strong currents, eddy shapes, inertial and internal tidal oscillations and mesoscale and submesoscale motions) and ice floe characteristics (e.g. shapes, thickness, surface topography, rheology, deformation and thermodynamics). Nonetheless, this study lays a foundation for a robust framework to characterise eddies from satellite remote sensing observations of sea ice motion, which can easily be extended beyond the BG to include MIZ eddies in the Arctic and Antarctic Oceans.

Supplementary movies. Supplementary movies are available at https://doi.org/10.1017/jfm.2025.10213.

Acknowledgements. M.K. sincerely thanks Dr D. Watkins for his valuable discussions and insightful feedback.

Funding. M.K. and M.M.W. were supported by the Office of Naval Research (ONR) Arctic Program (N00014-20-1-2753, N00014-22-1-2741 and N00014-22-1-2722). MMW was also supported by the National Aeronautics and Space Administration Science of Terra, Aqua, and Suomi-NPP Program (80NSSC22K0620). M.K., M.M.W., and G.E.M. were all supported by the ONR Multidisciplinary University Research Initiatives Program (N00014-23-1-2014) and the ONR Young Investigator Program (N00014-24-1-2283). This research used computational resources and services at the Center for Computation and Visualization, Brown University.

Declaration of interests. The authors report no conflict of interest.

Appendix A. Identification of ice floes trapped by an ocean eddy

We leverage ice floe trajectories resembling closed loops to identify floes trapped in an eddy core, in agreement with conventional eddy detection algorithms (Chelton *et al.* 2011; Mason *et al.* 2014). Several physical criteria were established for selecting closed-loop trajectories based on previous work using processed satellite remote sensing observations via the ice floe tracker algorithm (Lopez-Acosta *et al.* 2019; Lopez-Acosta 2021). First, the curvatures of all daily segments along the trajectory must be of the same sign, indicating that an ice floe has been rotating clockwise or counterclockwise. Then, considering a nominal eddy size of 20 km, trajectory curvatures are evaluated as they should surpass a predefined threshold typically set at 0.05 (km^{-1}). A third condition is set by the ratio of the arc length along the trajectory to the distance between the initial and final points. This value must exceed a specific threshold, typically set at 3, based on the geometry of a half-closed circular loop. Finally, only trajectories with lifetimes greater than four simulation days are considered to ensure adequate data points. Only trajectories meeting all four criteria are classified as closed-loop trajectories.

Appendix B. Effects of ice–ocean stress parametrisation on the relationship between ocean vorticity and the rotation rate of ice floes

The idealised Rankin (RK) vortex was used to examine the effect of ice–ocean stress on the rotational relationship between ice floes and the underlying ocean. In the RK vortex,

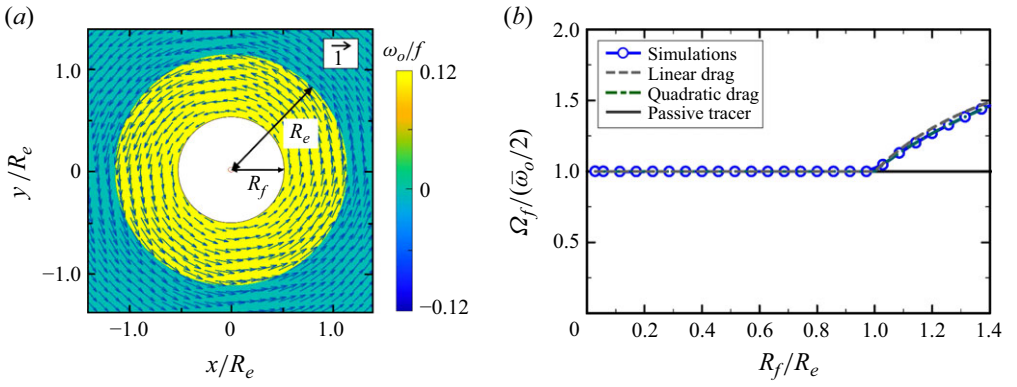

Figure 17. Motions of ice floes in a RK vortex field. (*a*) An ice floe (white circle) positioned at the centre of the vortex core (yellow region), with a floe–eddy size ratio of $R_f/R_e = 0.5$. The colours and arrows in the figure correspond to the magnitude of the vorticity normalised by the Coriolis parameter and the magnitude and direction of the velocity at a given location, respectively. (*b*) Rotation rates of the ice floe normalised by the averaged ocean vorticity over the floe area for different floe–eddy size ratios. The simulation results are compared with the analytical relations derived using the linear (dashed line) and quadratic (dashed-dotted line) drag laws, as well as with the passive tracer case (solid line).

vorticity remains constant within the core region ($r \leqslant R_e$) and is zero in the outer region. The velocity field is defined as $u_\theta = \Omega_f r$ for $r \leqslant R_e$ and $u_\theta = \Omega_f (R_e^2/r)$ for $r > R_e$, where u_θ is the azimuthal velocity. By representing the sea ice-ocean drag term using a linear drag law in (2.8) and (2.10), we can derive the relation for ice floe rotation as follows:

$$\Omega_f = \frac{\overline{\omega}_o}{2} \quad \text{for } R_f \leqslant R_e, \qquad \Omega_f = \frac{\overline{\omega}_o}{2}\left[2 - \left(\frac{R_e}{R_f}\right)^2\right] \quad \text{for } R_f > R_e, \tag{B1}$$

where $\overline{\omega}_o$ is the spatially averaged ocean vorticity over the floe area. For $R_f \leqslant R_e$, $\overline{\omega}_o = 2\Omega_f$, whereas for $R_f > R_e$, $\overline{\omega}_o = 2\Omega_f (R_e/R_f)^2$. These relations suggest that when $R_f \leqslant R_e$, the rotation of the ice floe mirrors the average rotation of the underlying eddies, akin to the passive tracer case. However, when $R_f > R_e$, the rotation rate increases and tends to converge toward twice the averaged ocean rotation as R_f approaches infinity. With the quadratic drag law (2.6), the rotation rate of ice floes remains unchanged compared with the linear parameterisation, provided that $R_f \leqslant R_e$. For $R_f > R_e$, the rotation rate of ice floes can be determined by solving the following algebraic equation:

$$\Omega_f^{5/2} - \Omega_f^{3/2}\left(\frac{\overline{\omega}_o}{2}\right)\left[\frac{10}{3} + \frac{4}{3}\left(\frac{R_e}{R_f}\right)^3\right] + \Omega_f^{1/2}\left(\frac{\overline{\omega}_o}{2}\right)^2\left[4\left(\frac{R_e}{R_f}\right) + 5\right] - \frac{16}{3}\left(\frac{\overline{\omega}_o}{2}\right)^{5/2} = 0, \tag{B2}$$

where $\Omega_f = \overline{\omega}_o/2$ for $R_f = R_e$. The quadratic drag parameterisation exhibits a closer fit to the simulation results compared with a linear drag (figure 17). However, the analytical relations demonstrate minimal dependence on drag parametrisations, as evidenced by the marginal error in the linear drag case.

References

Abernathey, R. & Haller, G. 2018 Transport by Lagrangian vortices in the eastern Pacific. *J. Phys. Oceanogr.* **48** (3), 667–685.

Adrian, R.J. & Westerweel, J. 2011 *Particle Image Velocimetry*. Cambridge University Press.

Aksamit, N.O., Encinas-Bartos, A.P., Haller, G. & Rival, D.E. 2024 Relative fluid stretching and rotation for sparse trajectory observations. *J. Fluid Mech.* **996**, A40.

Allende, S. & Bec, J. 2023 Velocity and acceleration statistics of heavy spheroidal particles in turbulence. *J. Fluid Mech.* **967**, R4.

von Appen, W.-J., Baumann, T.M., Janout, M., Koldunov, N., Lenn, Y.-D., Pickart, R.S., Scott, R.B. & Wang, Q. 2022 Eddies and the distribution of eddy kinetic energy in the Arctic Ocean. *Oceanography* **3** (4), 42–51.

Arbic, B.K., Scott, R.B., Flierl, G.R., Morten, A.J., Richman, J.G. & Shriver, J.F. 2012 Nonlinear cascades of surface oceanic geostrophic kinetic energy in the frequency domain. *J. Phys. Oceanogr.* **42** (9), 1577–1600.

Armitage, T.W.K., Manucharyan, G.E., Petty, A.A., Kwok, R. & Thompson, A.F. 2020 Enhanced eddy activity in the Beaufort Gyre in response to sea ice loss. *Nat. Commun.* **11** (1), 761.

Boffetta, G. & Ecke, R.E. 2012 Two-dimensional turbulence. *Annu. Rev. Fluid Mech.* **44** (1), 427–451.

Bordoloi, A.D. & Variano, E. 2017 Rotational kinematics of large cylindrical particles in turbulence. *J. Fluid Mech.* **815**, 199–222.

Brandt, L. & Coletti, F. 2022 Particle-laden turbulence: progress and perspectives. *Annu. Rev. Fluid Mech.* **54** (1), 159–189.

Brenner, S., Horvat, C., Hall, P., Lo Piccolo, A., Fox-Kemper, B., Labbé, S. & Dansereau, V. 2023 Scale-dependent air-sea exchange in the polar oceans: floe-floe and floe-flow coupling in the generation of ice-ocean boundary layer turbulence. *Geophys. Res. Lett.* **50** (23), e2023GL105703.

Brenner, S., Rainville, L., Thomson, J., Cole, S. & Lee, C. 2021 Comparing observations and parameterizations of ice-ocean drag through an annual cycle across the Beaufort Sea. *J. Geophys. Res. Oceans* **126** (4), e2020JC016977.

Caflisch, R.E. 1998 Monte Carlo and quasi-Monte Carlo methods. *Acta Numerica* **7**, 1–49.

Callies, J. & Ferrari, R. 2013 Interpreting energy and tracer spectra of upper-ocean turbulence in the submesoscale range (1–200 km). *J. Phys. Oceanogr.* **43** (11), 2456–2474.

Cassianides, A., Lique, C. & Korosov, A. 2021 Ocean eddy signature on SAR-derived sea ice drift and vorticity. *Geophys. Res. Lett.* **48** (6), e2020GL092066.

Chelton, D.B., Schlax, M.G. & Samelson, R.M. 2011 Global observations of nonlinear mesoscale eddies. *Prog. Oceanogr.* **91** (2), 167–216.

Cole, S.T., Timmermans, M.-L., Toole, J.M., Krishfield, R.A. & Thwaites, F.T. 2014 Ekman veering, internal waves, and turbulence observed under Arctic sea ice. *J. Phys. Oceanogr.* **44** (5), 1306–1328.

Comiso, J.C. 2012 Large decadal decline of the Arctic multiyear ice cover. *J. Clim.* **25** (4), 1176–1193.

Covington, J., Chen, N. & Wilhelmus, M.M. 2022 Bridging gaps in the climate observation network: a physics-based nonlinear dynamical interpolation of Lagrangian ice floe measurements via data-driven stochastic models. *J. Adv. Model. Earth Syst.* **14** (9), e2022MS003218.

Dauxois, T., *et al.* 2021 Confronting grand challenges in environmental fluid mechanics. *Phys. Rev. Fluids* **6** (2), 020501.

Deng, R., Wang, C.-H. & Smith, K.A. 2006 Bubble behavior in a Taylor vortex. *Phys. Rev. E* **73** (3), 036306.

Dibarboure, G., *et al.* 2025 Blending 2D topography images from the Surface Water and Ocean Topography (SWOT) mission into the altimeter constellation with the Level-3 multi-mission Data Unification and Altimeter Combination System (DUACS). *Ocean Sci.* **21** (1), 283–323.

Dong, C., Liu, Y., Lumpkin, R., Lankhorst, M., Chen, D., McWilliams, J.C. & Guan, Y. 2011 A scheme to identify loops from trajectories of oceanic surface drifters: an application in the Kuroshio extension region. *J. Atmos. Ocean. Technol.* **28** (9), 1167–1176.

Feltham, D.L. 2008 Sea ice rheology. *Annu. Rev. Fluid Mech.* **40** (1), 91–112.

Ferrari, R. & Wunsch, C. 2009 Ocean circulation kinetic energy: reservoirs, sources, and sinks. *Annu. Rev. Fluid Mech.* **41** (1), 253–282.

Gimbert, F., Marsan, D., Weiss, J., Jourdain, N.C. & Barnier, B. 2012 Sea ice inertial oscillations in the Arctic Basin. *The Cryosphere* **6** (5), 1187–1201.

Gupta, M., Gürcan, E. & Thompson, A.F. 2024 Eddy-induced dispersion of sea ice floes at the marginal ice zone. *Geophys. Res. Lett.* **51** (2), e2023GL105656.

Gupta, M. & Thompson, A.F. 2022 Regimes of sea-ice floe melt: ice-ocean coupling at the submesoscales. *J. Geophys. Res. Oceans* **127** (9), e2022JC018894.

HAAS, C. & DRUCKENMILLER, M. 2009 Ice thickness and roughness measurements. In *Field Techniques for Sea Ice Research* (ed. H. Eicken, M. Salganek & C. Hap), vol. 3, chap. 2, pp. 49–116. University of Alaska Press.

HALLER, G. 2005 An objective definition of a vortex. *J. Fluid Mech.* **525**, 1–26.

HALLER, G., HADJIGHASEM, A., FARAZMAND, M. & HUHN, F. 2016 Defining coherent vortices objectively from the vorticity. *J. Fluid Mech.* **795**, 136–173.

HARMS, T.D., BRUNTON, S.L. & MCKEON, B.J. 2024 Lagrangian gradient regression for the detection of coherent structures from sparse trajectory data. *R. Soc. Open Sci.* **11** (10), 240586.

HORVAT, C., TZIPERMAN, E. & CAMPIN, J.-M. 2016 Interaction of sea ice floe size, ocean eddies, and sea ice melting. *Geophys. Res. Lett.* **43** (15), 8083–8090.

HUNKINS, K.L. 1974 Subsurface eddies in the Arctic Ocean. In *Deep-Sea Research*, vol. 21, pp. 1017–1033. Elsevier.

ISERN-FONTANET, J., FONT, J., GARCÍA-LADONA, E., EMELIANOV, M., MILLOT, C. & TAUPIER-LETAGE, I. 2004 Spatial structure of anticyclonic eddies in the Algerian basin (Mediterranean Sea) analyzed using the Okubo–Weiss parameter. *Deep-Sea Res. II: Top. Stud. Oceanogr.* **51** (25-26), 3009–3028.

JAYARAM, R., JIE, Y., ZHAO, L. & ANDERSSON, H.I. 2020 Clustering of inertial spheres in evolving Taylor–Green vortex flow. *Phys. Fluids* **32** (4), 043306.

JOHANNESSEN, J.A., *et al.* 1987 Mesoscale eddies in the Fram Strait marginal ice zone during the 1983 and 1984 Marginal Ice Zone Experiments. *J. Geophys. Res. Oceans* **92** (C7), 6754–6772.

KLEIN, P., LAPEYRE, G., SIEGELMAN, L., QIU, B., FU, L.-L., TORRES, H., SU, Z., MENEMENLIS, D. & LE GENTIL, S. 2019 Ocean-scale interactions from space. *Earth Planet. Sci.* **6** (5), 795–817.

KOZLOV, I.E., ARTAMONOVA, A.V., MANUCHARYAN, G.E. & KUBRYAKOV, A.A. 2019 Eddies in the Western Arctic Ocean from spaceborne SAR observations over open ocean and marginal ice zones. *J. Geophys. Res. Oceans* **124** (9), 6601–6616.

KOZLOV, I.E. & ATADZHANOVA, O.A. 2022 Eddies in the marginal ice zone of Fram Strait and Svalbard from spaceborne SAR observations in winter. *Remote Sens.* **14** (1), 134.

KOZLOV, I.E., PLOTNIKOV, E.V. & MANUCHARYAN, G.E. 2020 Brief Communication: Mesoscale and submesoscale dynamics in the marginal ice zone from sequential synthetic aperture radar observations. *The Cryosphere* **14** (9), 2941–2947.

KRISHFIELD, R.A., PROSHUTINSKY, A., TATEYAMA, K., WILLIAMS, W.J., CARMACK, E.C., MCLAUGHLIN, F.A. & TIMMERMANS, M.L. 2014 Deterioration of perennial sea ice in the Beaufort Gyre from 2003 to 2012 and its impact on the oceanic freshwater cycle. *J. Geophys. Res. Oceans* **119** (2), 1271–1305.

KUBRYAKOV, A.A., KOZLOV, I.E. & MANUCHARYAN, G.E. 2021 Large mesoscale eddies in the Western Arctic Ocean from satellite altimetry measurements. *J. Geophys. Res. Oceans* **126** (5), e2020JC016670.

KWOK, R. & ROTHROCK, D.A. 2009 Decline in Arctic sea ice thickness from submarine and ICESat records: 1958–2008. *Geophys. Res. Lett.* **36** (15), L15501.

LEPPÄRANTA, M. 2011 *The Drift of Sea Ice*. Springer Science & Business Media.

LIU, C., WANG, Q., DANILOV, S., KOLDUNOV, N., MÜLLER, V., LI, X., SIDORENKO, D. & ZHANG, S. 2024 Spatial scales of kinetic energy in the Arctic Ocean. *J. Geophys. Res. Oceans* **129** (3), e2023JC020013.

LIU, T. & ABERNATHEY, R. 2023 A global Lagrangian eddy dataset based on satellite altimetry. *Earth Syst. Sci. Data Discuss.* **2022** (4), 1–20.

LOPEZ-ACOSTA, R. 2021 Sea ice drift in Arctic marginal ice zones derived from optical satellite imagery. PhD thesis, University of California, USA.

LOPEZ-ACOSTA, R., SCHODLOK, M.P. & WILHELMUS, M.M. 2019 Ice Floe Tracker: an algorithm to automatically retrieve Lagrangian trajectories via feature matching from moderate-resolution visual imagery. *Remote Sens. Environ.* **234**, 111406.

MA, B., STEELE, M. & LEE, C.M. 2017 Ekman circulation in the Arctic Ocean: Beyond the Beaufort Gyre. *J. Geophys. Res. Oceans* **122** (4), 3358–3374.

MANUCHARYAN, G.E., LOPEZ-ACOSTA, R. & WILHELMUS, M.M. 2022 Spinning ice floes reveal intensification of mesoscale eddies in the western Arctic Ocean. *Sci. Rep.* **12** (1), 7070.

MANUCHARYAN, G.E. & MONTEMURO, B.P. 2022 Subzero: a sea ice model with an explicit representation of the floe life cycle. *J. Adv. Model. Earth Syst.* **14** (12), e2022MS003247.

MANUCHARYAN, G.E. & STEWART, A.L. 2022 Stirring of interior potential vorticity gradients as a formation mechanism for large subsurface-intensified eddies in the Beaufort Gyre. *J. Phys. Oceanogr.* **52** (12), 3349–3370.

MANUCHARYAN, G.E. & THOMPSON, A.F. 2022 Heavy footprints of upper-ocean eddies on weakened Arctic sea ice in marginal ice zones. *Nat. Commun.* **13** (1), 2147.

MASON, E., PASCUAL, A. & MCWILLIAMS, J.C. 2014 A new sea surface height–based code for oceanic mesoscale eddy tracking. *J. Atmos. Ocean. Technol.* **31** (5), 1181–1188.
MCPHEE, M.G. 2012 Advances in understanding ice–ocean stress during and since AIDJEX. *Cold Reg. Sci. Technol.* **76**, 24–36.
MONTEMURO, B.P. & MANUCHARYAN, G.E. 2023 Subzero: a discrete element sea ice model that simulates floes as evolving concave polygons. *J. Open Source Softw.* **8** (88), 5039.
MORTENSEN, P.H., ANDERSSON, H.I., GILLISSEN, J.J.J. & BOERSMA, B.J. 2007 Particle spin in a turbulent shear flow. *Phys. Fluids* **19** (7), 078109.
MOWLAVI, S., SERRA, M., MAIORINO, E. & MAHADEVAN, L. 2022 Detecting Lagrangian coherent structures from sparse and noisy trajectory data. *J. Fluid Mech.* **948**, A4.
MÜLLER, V., WANG, Q., KOLDUNOV, N., DANILOV, S., SIDORENKO, D. & JUNG, T. 2024 Variability of eddy kinetic energy in the Eurasian Basin of the Arctic Ocean inferred from a model simulation at 1-km resolution. *J. Geophys. Res. Oceans* **129** (3), e2023JC020139.
OKUBO, A. 1970 Horizontal dispersion of floatable particles in the vicinity of velocity singularities such as convergences. In *Deep-Sea Res*, vol. 17, pp. 445–454. Elsevier.
OUELLETTE, N.T., O'MALLEY, P.J.J. & GOLLUB, J.P. 2008 Transport of finite-sized particles in chaotic flow. *Phys. Rev. Lett.* **101** (17), 174504.
OUTRATA, O., PAVELKA, M., HRON, J., LA MANTIA, M., POLANCO, J.I. & KRSTULOVIC, G. 2021 On the determination of vortex ring vorticity using Lagrangian particles. *J. Fluid Mech.* **924**, A44.
PARSA, S., CALZAVARINI, E., TOSCHI, F. & VOTH, G.A. 2012 Rotation rate of rods in turbulent fluid flow. *Phys. Rev. Lett.* **109** (13), 134501.
PNYUSHKOV, A., POLYAKOV, I.V., PADMAN, L. & NGUYEN, A.T. 2018 Structure and dynamics of mesoscale eddies over the Laptev Sea continental slope in the Arctic Ocean. *Ocean Sci.* **14** (5), 1329–1347.
QIAO, J., DENG, R. & WANG, C.-H. 2014 Droplet behavior in a Taylor vortex. *Intl J. Multiph. Flow* **67**, 132–139.
QIAO, J., DENG, R. & WANG, C.-H. 2015 Particle motion in a Taylor vortex. *Intl J. Multiph. Flow* **77**, 120–130.
RAMPAL, P., WEISS, J. & MARSAN, D. 2009 Positive trend in the mean speed and deformation rate of Arctic sea ice, 1979-2007. *J. Geophys. Res. Oceans* **114** (C5), C05013.
ROLPH, R.J., FELTHAM, D.L. & SCHRÖDER, D. 2020 Changes of the Arctic marginal ice zone during the satellite era. *The Cryosphere* **14** (6), 1971–1984.
SHRESTHA, K. & MANUCHARYAN, G.E. 2022 Parameterization of submesoscale mixed layer restratification under sea ice. *J. Phys. Oceanogr.* **52** (3), 419–435.
STRONG, C. & RIGOR, I.G. 2013 Arctic marginal ice zone trending wider in summer and narrower in winter. *Geophys. Res. Lett.* **40** (18), 4864–4868.
ŠVANČARA, P., PAVELKA, M. & LA MANTIA, M. 2020 An experimental study of turbulent vortex rings in superfluid 4He. *J. Fluid Mech.* **889**, A24.
TAYLOR, J.R. & THOMPSON, A.F. 2023 Submesoscale dynamics in the upper ocean. *Annu. Rev. Fluid Mech.* **55** (1), 103–127.
TEE, Y.H. & LONGMIRE, E.K. 2024 Effect of fluid motions on finite spheres released in turbulent boundary layers. *J. Fluid Mech.* **985**, A28.
TIMMERMANS, M.-L. & MARSHALL, J. 2020 Understanding Arctic Ocean circulation: A review of ocean dynamics in a changing climate. *J. Geophys. Res. Oceans* **125** (4), e2018JC014378.
TIMMERMANS, M.-L., TOOLE, J., PROSHUTINSKY, A., KRISHFIELD, R. & PLUEDDEMANN, A. 2008 Eddies in the Canada Basin, Arctic Ocean, observed from ice-tethered profilers. *J. Phys. Oceanogr.* **38** (1), 133–145.
TULLOCH, R., MARSHALL, J., HILL, C. & SMITH, K.S. 2011 Scales, growth rates, and spectral fluxes of baroclinic instability in the ocean. *J. Phys. Oceanogr.* **41** (6), 1057–1076.
VARAKSIN, A.Y. & RYZHKOV, S.V. 2022 Vortex flows with particles and droplets (a review). *Symmetry* **14** (10), 2016.
VOTH, G.A. & SOLDATI, A. 2017 Anisotropic particles in turbulence. *Annu. Rev. Fluid Mech.* **49** (1), 249–276.
WATKINS, D.M., BLISS, A.C., HUTCHINGS, J.K. & WILHELMUS, M.M. 2023 Evidence of abrupt transitions between sea ice dynamical regimes in the East Greenland marginal ice zone. *Geophys. Res. Lett.* **50** (15), e2023GL103558.
WERELEY, S.T. & LUEPTOW, R.M. 1999 Inertial particle motion in a Taylor Couette rotating filter. *Phys. Fluids* **11** (2), 325–333.
YANG, J. 2006 The seasonal variability of the Arctic Ocean Ekman transport and its role in the mixed layer heat and salt fluxes. *J. Clim.* **19** (20), 5366–5387.
YUAN, D., HAO, Z., YOU, J., ZHANG, P., YIN, B., LI, Q. & XU, Z. 2023 Enhancing sea ice inertial oscillations in the Arctic Ocean between 1979 and 2019. *Water* **15** (1), 152.

ZHAO, L., CHALLABOTLA, N.R., ANDERSSON, H.I. & VARIANO, E.A. 2015 Rotation of nonspherical particles in turbulent channel flow. *Phys. Rev. Lett.* **115** (24), 244501.

ZHAO, M., TIMMERMANS, M.-L., COLE, S., KRISHFIELD, R., PROSHUTINSKY, A. & TOOLE, J. 2014 Characterizing the eddy field in the Arctic Ocean halocline. *J. Geophys. Res. Oceans* **119** (12), 8800–8817.

ZHAO, M., TIMMERMANS, M.-L., COLE, S., KRISHFIELD, R. & TOOLE, J. 2016 Evolution of the eddy field in the Arctic Ocean's Canada Basin, 2005–2015. *Geophys. Res. Lett.* **43** (15), 8106–8114.